A protein hydroxylase couples epithelial membrane biology to nucleolar ribosome biogenesis

Eline Hendrix[1,2#], Regina Andrijes[1,3#], Uncaar Boora[1], Arashpreet Kaur[1], James R Bundred[1,4], Leah Officer-Jones[5], Rachel Pennie[5], Ian R Powley[5], Adam Zayer[6,7], Raphael Heilig[8], Christian A E Westrip[1], Sally C Fletcher[1], Charlotte D Eaton[1,9], Tristan J Kennedy[1], Sonia Piasecka[1], Roman Fischer[8], Stephen J Smerdon[1], John Le Quesne[5,10,11], Mathew L Coleman[1§]

[1]Institute of Cancer and Genomic Sciences, University of Birmingham, Birmingham, UK
[2]Present address: Department of Biochemistry, Stanford University, Stanford, California, USA
[3]Present address: GSK, Gunnels Wood Rd, Stevenage, UK
[4]Present address: School of Medicine, University of Leeds, Woodhouse, Leeds, UK
[5]CRUK Beatson Institute, Garscube Estate, Glasgow, United Kingdom
[6]Centre for Cellular and Molecular Physiology, University of Oxford, Headington, Oxford, UK
[7]Thermo Fisher Scientific, Cambridge, UK
[8]Target Discovery Institute, Nuffield Department of Medicine, NDM Research Building, University of Oxford, Old Road Campus, Roosevelt Drive, Headington, Oxford, UK
[9]Present address: School of Medicine, UCSF, San Francisco, USA
[10]School of Cancer Sciences, University of Glasgow, Glasgow, United Kingdom.
[11]Department of Histopathology, Queen Elizabeth University Hospital, Glasgow, United Kingdom.
[§]To whom correspondence should be addressed: *m.coleman@bham.ac.uk*
[#]These authors contributed equally

Abstract

Jumonji-C (JmjC) ribosomal protein hydroxylases are an ancient class of oxygen- and Fe(II)-dependent oxygenases that spawned the wider JmjC family and Histone Lysine Demethylases (KDMs) in eukaryotes. Myc-induced Antigen (MINA) has been implicated in ribosome biogenesis and was assigned as a nucleolar-localized JmjC histidyl hydroxylase of the large ribosomal subunit protein RPL27A, consistent with reports that it supports cell growth and viability in a variety of tumor cell types. Reported roles in diverse aspects of disease biology may be consistent with additional MINA functions, although the molecular mechanisms involved remain unclear. Here, we describe an extra-nucleolar interaction of MINA with the Hinge domain of the membrane-associated guanylate kinase, MPP6. We show that MINA promotes the expression and membrane localization of MPP6 and that the MINA-MPP6 pathway is required for epithelial tight junction integrity and barrier function. The function of MINA in this novel pathway is suppressed by ribosomal RNA transcription and the nucleolar MINA interactome. In this way, MINA couples epithelial membrane biology to nucleolar ribosome biogenesis. Our work sheds light on how quiescent cells lose adhesion as they switch to proliferative states associated with increased ribosome biogenesis.

Keywords: Myc, ribosome biogenesis, tight junction, polarity, barrier function, RNA polymerase I, protein hydroxylase, MAGUK, polarity

Introduction

Cross-talk between cellular processes is key to enabling a coordinated multisystem response to a change in cell fate. The switch to a proliferative state requires increased metabolic activity and accumulation of biomass to feed cell growth and cell cycle-dependent changes in adhesion to support division[1-3]. Cells have evolved sophisticated signaling mechanisms to couple such processes. For example, bidirectional cross-talk has been demonstrated between cell adhesion and the cell cycle[3]. Whether cell adhesion is coupled to other fundamental processes linked to growth remains unclear.

Ribosomal RNA (rRNA) synthesis is a rate-limiting step of ribosome biogenesis and is upregulated as cells switch from growth-arrested to proliferative states in response to major growth responsive signaling pathways and transcription factors, such as Myc[2,4]. Activation of Myc or the RNA polymerase I (RNApol1) transcription initiation factor RRN3 is sufficient to induce RNApol1 activity and proliferation in human epithelial cells[5-8]. Remarkably, normal 3D morphogenesis (which requires functional polarity and adhesion) is impaired under such conditions[7,8], suggesting that ribosome biogenesis, like the cell cycle, might also be coupled to epithelial membrane biology in some way.

MINA is a nucleolar-localized Myc target gene implicated in ribosome biogenesis[9-11]. It is a member of the 2-oxoglutarate (2OG)-, Fe(II)-, and oxygen-dependent oxygenase family, and is highly related to NO66, a prokaryotic orthologue of which is believed to have evolved into the eukaryotic JmjC enzymes, including KDMs[12]. Despite the presence of a JmjC catalytic domain, detailed structural and biochemical studies suggest that MINA and NO66 may not be KDMs[12]. Indeed, they catalyze non-redundant and site-specific histidine hydroxylation of the large ribosomal subunit proteins RPL27A and RPL8, respectively[13]. Hydroxylation has been proposed to support the optimal conformation of the target residue to promote its interaction with rRNA[14]. Consistent with a positive role in ribosome biogenesis/function, multiple studies have described upregulation of MINA in rapidly growing cells, including in tumors (reviewed in[11]). However, recent reports have also implicated MINA in suppressing cell migration, invasion, and epithelial-to-mesenchymal transition (EMT)[15,16]. How MINA controls these aspects of epithelial biology, and whether it is independent of, or may be coupled to, its role in nucleolar ribosome biogenesis, remains unclear.

Here, we describe a novel extra-nucleolar function for MINA in epithelial barrier function through its pseudosubstrate-like interaction with MPP6, a member of the 'palmitoylated membrane protein' (MPP) subfamily of the MAGUK superfamily of cell adhesion and polarity adaptor proteins. Furthermore, we provide evidence suggesting that increased RNAPol1

activity sinks MINA into the nucleolus to suppress the role of MINA in cell adhesion, thereby coupling ribosome biogenesis to epithelial membrane biology.

Results

MINA promotes epithelial barrier function

Although MINA has been implicated as an oncogenic driver of tumor proliferation, there is emerging literature on its role in suppressing cell migration and invasion. However, these functional studies have generally focused on the role of MINA in highly proliferative cells that have undergone a robust EMT, such as rapidly proliferating tumor cell lines[11] and references therein)). MINA is ubiquitously expressed in normal healthy human tissues (Figure S1), and yet its role in such contexts is poorly characterized. To begin to explore its physiological role in more detail we studied MINA in intestinal epithelial cells that retain good cell adhesion, polarity, and barrier function, and that can differentiate and undergo morphogenesis in 3D[17,18]. As such, we generated Caco-2 cell lines stably expressing doxycycline-inducible MINA shRNA sequences. In these cells MINA depletion did not affect proliferation (Figure S2) or grossly alter apico-basal asymmetry, as assessed by the localization of tight and adherens junction markers ZO-1 and E-cadherin, respectively (Figure 1A). However, we observed an increase in cell perimeter and cell flattening following MINA knockdown (Figures 1A and 1B). MINA depletion also resulted in delayed formation of transepithelial electrical resistance (TEER; Figure 1C) and a reduction in ‘domes’ (Figures 1D and 1E), which are normally formed when fluid is pumped under a cell monolayer, in the context of good cell:cell adhesion. Taken together, these data suggest that MINA may be required for tight junction (TJ) integrity and barrier function[19,20]. Consistent with this hypothesis, we noted reduced membrane localization and expression of tight junction-associated protein Claudin-1 in response to MINA depletion (Figures 1F, 1G and 1H). How a nucleolar ribosomal protein hydroxylase regulates such membrane-related biology is unclear.

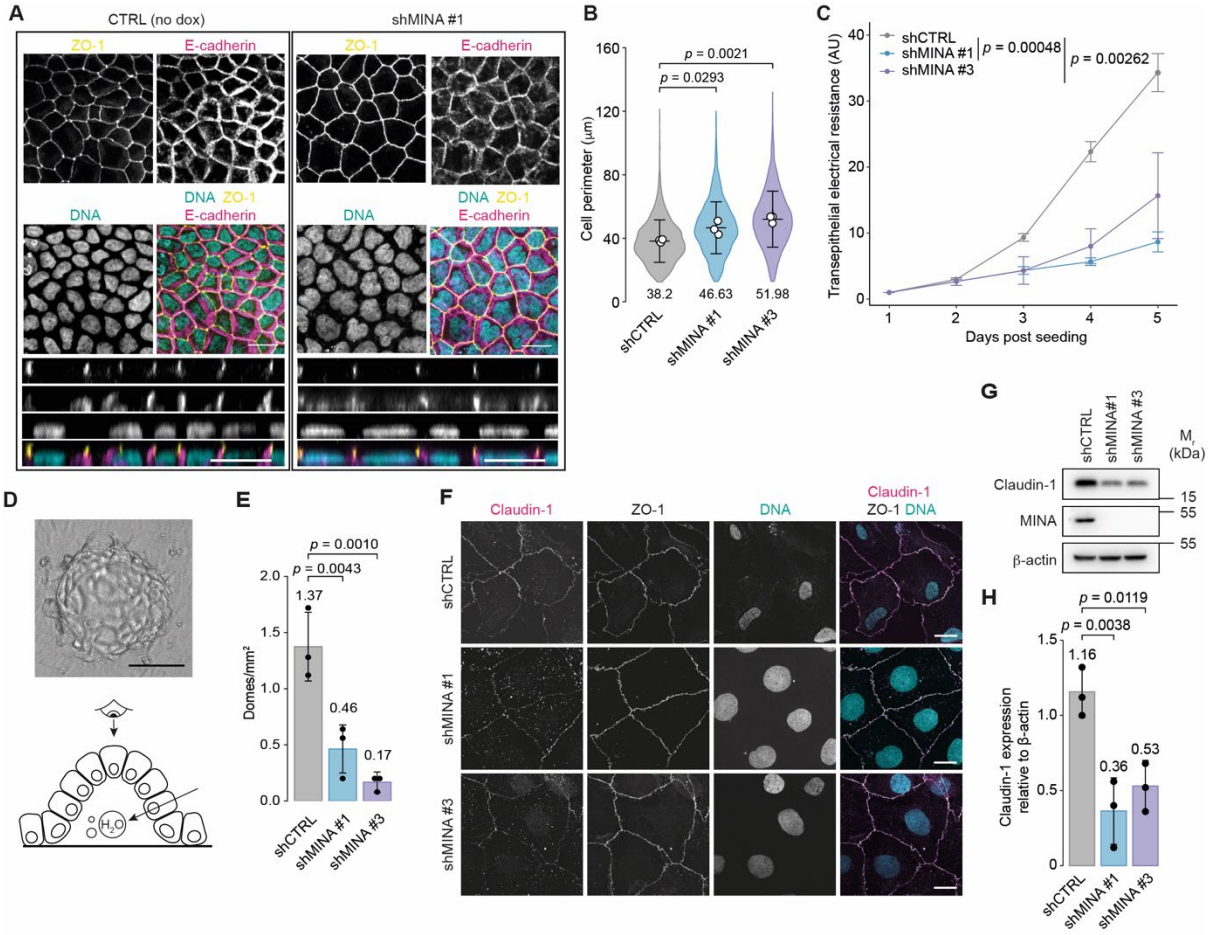

Figure 1. MINA promotes tight junction integrity and epithelial barrier function

(A) *Increased perimeter of cells in MINA-depleted monolayers. Caco-2 cells expressing a non-targeting (shCTRL) or MINA-targeting shRNA (shMINA#1) were grown on a semi-permeable membrane for 10 days and stained for ZO-1 (yellow), E-cadherin (magenta) and DNA (DAPI, cyan). Consecutive images were taken from the basal to the apical side and presented as a maximum projection image (top panels) or orthogonal view (rectangular bottom panels). Orthogonal views show the basal side at the bottom and apical side (as indicated by ZO-1) at the top. Scale bars, 20 µm.*

(B) *Quantification of cell perimeters under conditions presented in (A). Violin plot represents the data from 3 independent experiments. n = 4572 (shCTRL), 2616 (shMINA #1) and 2426 (shMINA #3) cells. The average of each condition is shown underneath each respective violin.*

(C) *Delayed establishment of transepithelial electrical resistance (TEER) in MINA-depleted cells. Monolayer integrity and permeability were analyzed on the indicated days by measuring the electrical resistance across the monolayer. Line graph shows the average of three technical repeats of one representative biological experiment. The experiment was repeated 5 times with similar results.*

(D) *Top, phase-contrast image of a dome, as viewed from the top. Scale bar, 100 µm. Bottom, illustration of a dome, as viewed from the side.*

(E) *Quantification of dome formation in monolayers of stable Caco-2 cells expressing the indicated shRNA sequences. Bars represent the average number of domes per mm^2 of n = 3 independent experiments. The average of each condition is shown above each respective bar.*

(F) *Altered localization of tight junction protein Claudin-1 following MINA knockdown.*

Representative images of Caco-2 monolayers expressing the indicated shRNAs were stained for Claudin (magenta), ZO-1 (gray) and DNA (DAPI; cyan). Scale bars, 20 µm.
(G) *Reduced Claudin-1 protein expression in response to MINA knockdown. Extracts from Caco-2 cells expressing the indicated shRNA sequences were grown into a monolayer over 5 days and immunoblotted for Claudin-1 (23 kDa) and MINA (53 kDa). β-actin was used as loading control. Uncropped images are shown in source data.*
(H) *Quantification of (G). Bar graph shows Claudin-1 expression relative to β-actin. Bars represent the average of n = 3 biological repeats.*
(B), (C), (E), and (H); Statistical significance was determined using a one-way analysis of variance (ANOVA) and p values were calculated post-hoc using a Dunnett's test for multiple comparisons. Error bars, standard deviation (SD).

MINA nucleolar localization is dependent on its nucleolar interactome and elevated ribosome biogenesis

To investigate the role of MINA in epithelial membrane biology we first re-evaluated its subcellular localization. Consistent with reports describing nucleolar MINA staining in highly proliferative normal tissues, such as the testes[21], and in tumors (reviewed in[11]), we observed strong nucleolar enrichment of MINA in rapidly growing mesenchymal-like cell lines (e.g. SW620 and A549; Figure 2A). Surprisingly, this enrichment was diminished in slower growing cell lines with a more epithelial morphology. In U2OS and Caco-2 cells the localization of MINA appeared heterogenous with some cells showing diffuse nucleoplasmic staining and no nucleolar enrichment (Figures 2A and S3A).

We hypothesized that the subcellular localization of MINA might be related to growth status. To test this, we cultured Caco-2 to either subconfluence or confluence (Figure 2B and 2C): In subconfluent cells we observed a more homogenous subcellular distribution of MINA with diffuse nucleoplasmic staining *and* nucleolar enrichment. In confluent cells MINA distributed evenly throughout the nucleus without any nucleolar enrichment (Figure 2B and 2C). To explore the physiological relevance of pan-nuclear MINA localization we developed an automated and quantitative multiplex immunofluorescence assay for staining MINA and nucleoli in normal human colon (Figure 2D). Consistent with our observations in confluent Caco-2 cells, we observed pan-nuclear MINA staining across intestinal crypts and villi (Figure 2E). Quantitative analyses using nuclear (DAPI) and nucleolar (UBF1) markers indicated that the nucleolar:nuclear ratio of MINA staining intensity was close to 1 (Figure 2F and 2G), confirming pan-nuclear localization in healthy intestinal epithelium.

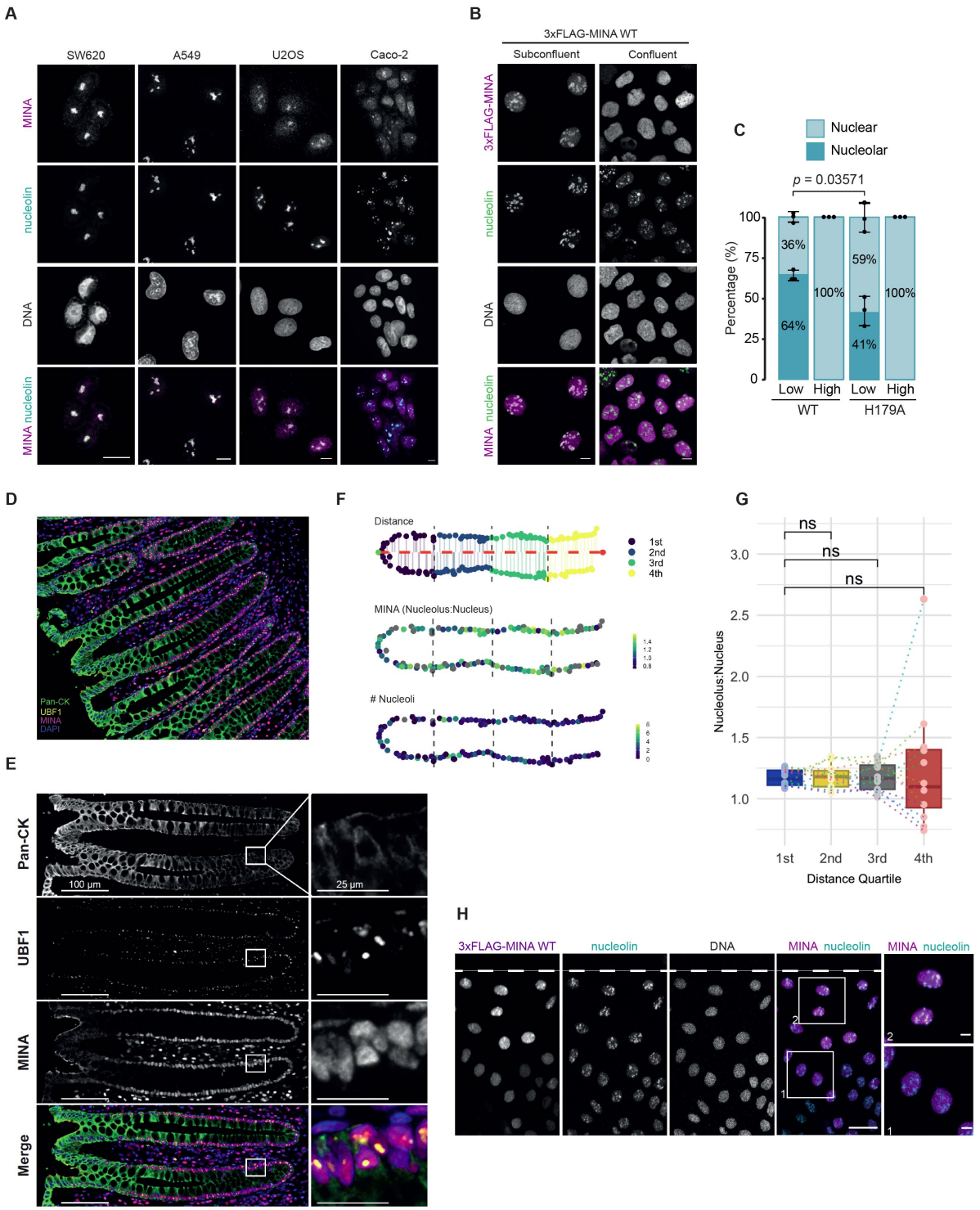

Figure 2. MINA nucleolar localization is regulated by growth and hydroxylase activity

(A) *Localization of MINA in selected cancer cell lines. Representative immunofluorescence images showing nucleolar and/or nucleoplasmic MINA. Cells were fixed with methanol and stained for endogenous MINA (magenta) and the nucleolar marker nucleolin (cyan). Scale bars, 10 µm.*

(B) *Nucleolar MINA localization depends on cell confluence. Representative immunofluorescence images showing the localization of wildtype (WT) 3xFLAG-MINA in subconfluent and confluent conditions. Cells were incubated with 0.1 µg/mL doxycycline for*

48 h to induce expression of 3xFLAG-MINA and stained with an antibody raised against endogenous MINA (magenta). To confirm that the detected signal was of overexpressed, exogenous 3xFLAG-MINA, an empty vector control was used (Figure S3B). Cells were counterstained for nucleolin (NCL, green) and DNA (DAPI, gray). Scale bars, 10 µm

(C) *Bar graph showing the percentage of cell in which nucleolar enrichment could ('Nucleolar') or could not ('Nuclear') be observed. 'Low' and 'High' refer to the level of confluence. Bars show the average of three biological repeats. Error bars, SD. A total of one hundred cells were counted per condition per experiment. Samples were blinded before analysis. Statistical significance was determined using an unpaired t-test.*

(D) *Localization of MINA in normal human colon. Representative multiplexed immunofluorescence image showing MINA (magenta), epithelial cell marker pan-cytokeratin (green) and the nucleolar marker UBF1 (yellow).*

(E) *Representative immunofluorescence images showing the localization of MINA, pan-cytokeratin and the nucleolar marker UBF1 in normal human colonic crypts. Enlargements show nuclear detail with pan-nuclear MINA localization. Note the loss of MINA staining intensity in the differentiated cells of the villi.*

(F) *Nucleolar number, nucleoplasm and nucleolar MINA expression were quantified at the cellular level (n = 12 crypts) and crypts divided into quartiles based on their distance from the crypt base. Nucleolus:Nuclear ratio calculated as mean nucleolar per pixel intensity divided by mean nucleoplasm per pixel intensity. Nucleoli # represents number of nucleolar quantified per cell nucleus.*

(G) *Per cell Nucleolus:nuclear MINA expression were calculated as in (F) and binned per quartile along the crypt axis. Mean values were calculated per crypt (n=12, represented as points). Box plots represent median values with hinges corresponding to the first and third quartiles and whiskers extending to no further than 1.5* the interquartile range from the hinge. ns represents non-significant (p>0.05) difference from paired Wilcoxon test.*

(H) *MINA becomes enriched in the nucleolus following disruption of a confluent monolayer. A scratch was introduced to disrupt a confluent monolayer of Caco-2 cells expressing wildtype 3xFLAG-MINA. Cells were fixed 24 h after the scratch was made. Re-localization of 3xFLAG-MINA was observed in cells proximal to the scratch (top, indicated by the white dashed line). In contrast, at a distance from the scratch, 3xFLAG-MINA remained in the nucleoplasm (bottom). Scale bars, 50 or 10 (enlargements) µm.*

To explore whether MINA localization is dynamic and responds to external cues we grew Caco-2 cells to confluence before scratching the monolayer. As expected, confluent cells distal to the scratch showed pan-nuclear MINA localization. However, cells proximal to the scratch showed elevated levels of MINA and nucleolar enrichment (Figure 2G). The nucleolar enrichment of overexpressed MINA was partly dependent on its catalytic, suggesting a role for RPL27A hydroxylation (Figures 2C and S3B).

Considering the importance of MINA hydroxylase activity, and the established links between growth and ribosome biogenesis, we hypothesized that high levels of ribosome biogenesis might act as a nucleolar sink for MINA. Consistent with this possibility, we observed significant

214 nucleolar enrichment of nascent proteins that colocalized with MINA in subconfluent cells
215 (Figure 3A). Under these conditions, inhibition of rRNA transcription and ribosome biogenesis
216 with RNAPol1 inhibitors was sufficient to redistribute MINA from the nucleolus to the
217 nucleoplasm (Figures 3B and S4A)[9]. Publicly available SILAC proteomic data demonstrate
218 that the response to RNAPol1 inhibition is rapid and dynamic (Figure 3C)[22]. Conversely,
219 overexpression of the RNAPol1 activator RRN3 was sufficient to enrich some MINA in the
220 nucleoli of confluent cells (Figure S4B). Nucleophosmin (NPM1) is a highly abundant nucleolar
221 protein involved in ribosome biogenesis and a major MINA-binding partner[9,13]. To test whether
222 NPM1 contributes to nucleolar sequestration of MINA we targeted it with siRNA in
223 subconfluent Caco-2 cells. Consistent with the hypothesis, loss of NPM1 expression was
224 sufficient to redistribute MINA to the nucleoplasm (Figure S4C). Overall, our localization
225 analyses suggest that nucleolar enrichment of MINA is dependent on elevated levels of
226 ribosome biogenesis and its nucleolar interactome. In cells where these determinants are lost
227 or suppressed, MINA is redistributed to the nucleoplasm, where (we hypothesize) it
228 undertakes an alternative function in epithelial membrane biology.

229 We reasoned that a nucleolar localization mutant would support efforts to dissect nucleolar
230 versus extra-nucleolar MINA functions. We searched the MINA primary sequence for
231 nucleolar localization sequences (NoLSs)[23] and identified two potential candidates, one at the
232 N-terminus and a bipartite-like motif within residues 100-125 (Figure S5A). The latter was
233 more highly conserved than the N-terminal sequence (Figure S5B). The basic residues at the
234 C-terminal end of the conserved bipartite motif (R125/K126) are within an a-helix and their
235 side chains are solvent-exposed, which are known determinants of NoLSs (Figure 3D)[24]. The
236 C-terminal part of bipartite NoLSs have previously been shown to be involved in nucleolar
237 targeting[24]. Therefore, we considered R125/K126 as residues of interest to experimentally test
238 their contribution to MINA nucleolar localization. Consistent with predictions, an
239 R125G/K126G mutant (NoLS) was unable to localize to the nucleolus (Figure 3E) and did not
240 interact with the nucleolar targets RPL27A and NPM1 (Figure 3F). The R125G/K126G
241 mutation retained nuclear localization (Figure 3E) and hydroxylase activity (Figure S5C),
242 suggesting that MINA NoLS mutant is a viable tool for investigating the extra-nucleolar role of
243 MINA.

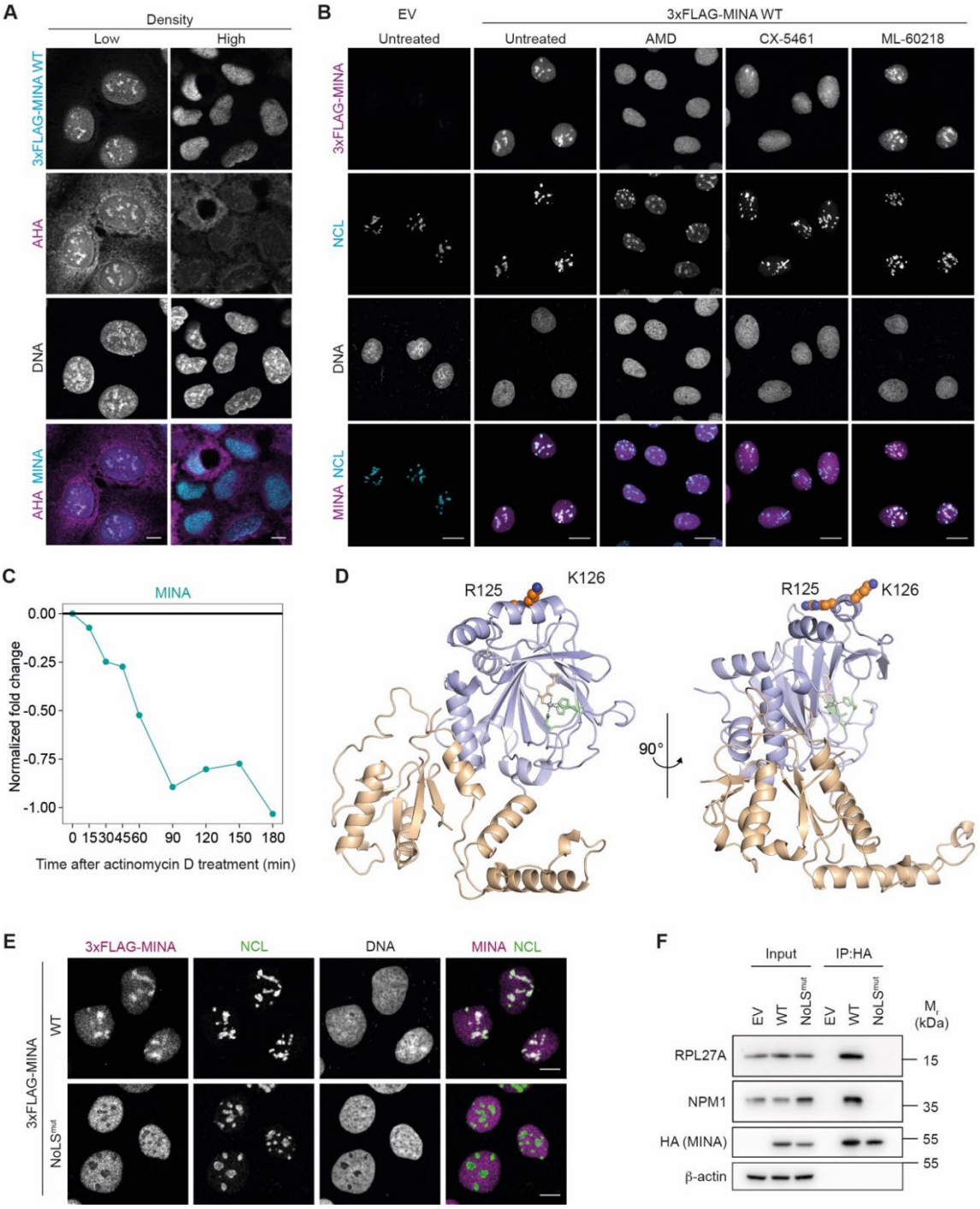

Figure 3. Determinants of subnuclear MINA localization

(A) *3xFLAG-MINA colocalizes with newly synthesized proteins in the nucleoli of subconfluent cells. Stable Caco-2 cells expressing wildtype (WT) 3xFLAG-MINA and seeded at a high or low density were treated with methionine analogue L-Azidohomoalanine (AHA, magenta) for 1 h before the cells were fixed and labelled using Click-IT chemistry. Cells were co-stained for MINA (cyan). Scale bars, 10 µm.*

(B) *Nucleoplasmic translocation of MINA in response to RNA polymerase I inhibitors. Expression of 3xFLAG-MINA was induced in subconfluent Caco-2 cells using 0.1 µg/mL doxycycline for 48 h prior to treatment. Empty vector (EV) or WT 3xFLAG-MINA expressing cells were either untreated or treated with 40 ng/mL actinomycin D (AMD) or CX-5461 to inhibit*

RNA polymerase I for 4 h. Parallel samples were treated with RNA polymerase III inhibitor ML-60218 to determine the specificity of the observed effects. Cells were stained for MINA (magenta), nucleolin (NCL, cyan) and DNA (DAPI, gray). Scale bars, 20 µm.
(C) *SILAC proteomic data demonstrate that the nucleolar abundance of MINA declines rapidly in response to actinomycin D (see Anderson et al, main text ref [22]). The authors treated HeLa cells with 1 µg/mL actinomycin D for the indicated times before mass spectrometry-based quantification of the nucleolar proteome.*
(D) *Ribbon representation of a MINA monomer showing residues that contribute to MINA nucleolar localization (R125/K126) and the catalytic core in purple. Protein Data Bank (PDB) ID = 4BXF. Structures were visualized using PyMOL.*
(E) *R125G/K126G mutations prevent MINA nucleolar localization. Caco-2 cells expressing either WT or 3xFLAG-MINA R125G/K126G (NoLS^{mut}) were stained for MINA (magenta), nucleolar protein nucleolin (NCL, green) and DNA (DAPI, gray). Scale bars, 10 µm. Expression of 3xFLAG-MINA was induced by treatment with 0.1 µg/mL doxycycline for 48 h.*
(F) *MINA NoLS^{mut} does not interact with nucleolar interactors RPL27A and NPM1. Anti-HA immunoprecipitates (IP) from extracts of HEK293T cells transiently expressing the indicated HA-MINA constructs were immunoblotted for RPL27A (17 kDa), NPM1 (33 kDa) and HA (MINA, 53 kDa). β-actin (42 kDa) was used as loading control. Input = cell extract prior to immunoprecipitation (for RPL27A and NPM1 the input is 1% of the IP, for HA and β-actin it is 50%). β-actin (42 kDa) was used as loading control. Uncropped western blot images are presented in source data.*

Extra-nucleolar MINA interacts with membrane palmitoylated protein 6 (MPP6)

To investigate how extra-nucleolar MINA regulates barrier function we next sought to identify extra-nucleolar MINA interactors. We hypothesized that a physiologically relevant extra-nucleolar MINA interactor might exist in multiple independent cell types and be enriched in NoLS versus wildtype MINA pulldowns. Therefore, we first immunopurified wildtype 3xFLAG-MINA from three diverse cell types (Caco-2, U2OS, and mouse embryonic fibroblasts) before trypsinolysis and MS-based protein identification. We removed contaminants present in control samples before applying strict filtering criteria to identify only the highest confidence and most abundant interactors. Cross-referencing the three datasets identified just four proteins in common, two of which were the known interactors RPL27A and NPM1. Next, we compared NoLS and wildtype MINA proteomic screens performed in Caco-2 cells to identify proteins with increased binding to extranucleolar MINA: We cross-referenced these candidates with the four proteins identified in multiple cell lines above, which identified one protein, MPP6 (Figure 4A). Because MPP6 is a member of the MAGUK superfamily of cell adhesion and polarity proteins (Figure S6)[25], we considered it a viable candidate to mediate the extra-nucleolar functions of MINA in epithelial membrane biology. Therefore, we sought to study the MINA:MPP6 interaction in more detail.

296 First, we independently validated the proteomic results in multiple cell types (Figures 4B, S7A
297 and S7B). As expected, we observed a specific interaction between MPP6 and MINA that was
298 increased in the nucleolar localization mutant. Intriguingly, the interaction was dependent on
299 the catalytic activity of MINA, being completely abolished by an inactivating Fe(II)-binding
300 mutation (H179A) (Figures 4B, S7A and S7B) (the role of MINA activity is investigated in more
301 detail below). Next, we explored the specificity of the MINA:MPP6 interaction. Under
302 conditions where endogenous MPP6 interacted with HA-MINA, it did not bind to the closely
303 related hydroxylase NO66 (Figure S7C). Similarly, FLAG-MINA coprecipitates with MPP6-HA,
304 but not with the highly related MPP2 (sequence identity = 65.2%) (Figure S7D). Endogenous
305 MPP6 coprecipitates endogenous MINA (Figure S7E). Consistent with the MINA localization
306 (Figure 1) and proteomic analyses (Figure 4), immunofluorescence and proximity ligation
307 assays (PLA) indicate that 3xFLAG-MINA and MPP6-HA colocalize and interact in the
308 nucleoplasm of subconfluent cells (Figures 4C and Figure S7F). Moreover, the PLA signal
309 was reduced in confluent monolayers (Figure 4C), consistent with the translocation of MPP6
310 from the nuclear compartment to the membrane (Figure S7G). Unsurprisingly therefore, less
311 MPP6 interacts with 3xFLAG-MINA in highly confluent monolayers of Caco-2 (Figure S7H).
312 Increasing the pool of extra-nucleolar MINA in subconfluent cells (through RNApol1 inhibition,
313 Figure 1) increased its interaction with MPP6 (Figure 4D). The NoLS mutant showed
314 constitutively increased MPP6 binding, as expected, and was completely resistant to the
315 effects of RNApol1 inhibition (Figure 4D). These data indicate that RNApol1 activity and
316 ribosome biogenesis sequester MINA in the nucleolus of subconfluent cells, thereby
317 suppressing its interaction with MPP6.

318

319 **The Hinge regions of MPP2 and MPP6 confer MINA binding specificity**

320 As scaffold proteins, MAGUK proteins are characterized by the presence of several protein-
321 protein interaction domains. These include a characteristic PDS-95/DLG/ZO-1 (PDZ) – Src
322 homology 3 (SH3) – guanylate kinase (GUK) tandem motif ('PSG') (Figure S6) that can fold
323 into a structural supramodule[26]. Folding requires a disordered 'Hinge' region that loops out of
324 the non-canonical SH3 domain and that includes a polybasic sequence implicated in
325 membrane localization and protein:protein interactions[27]. Modeling the tertiary structure of
326 MPP6 using AlphaFold confirms the likelihood that the PDZ, SH3, and GUK domains of MPP6
327 form a PSG supramodule analogous to ZO-1 (Figure 4E). Furthermore, the AlphaFold model
328 of MPP6 also predicts the presence of a Hinge insert within its non-canonical split SH3
329 domain.

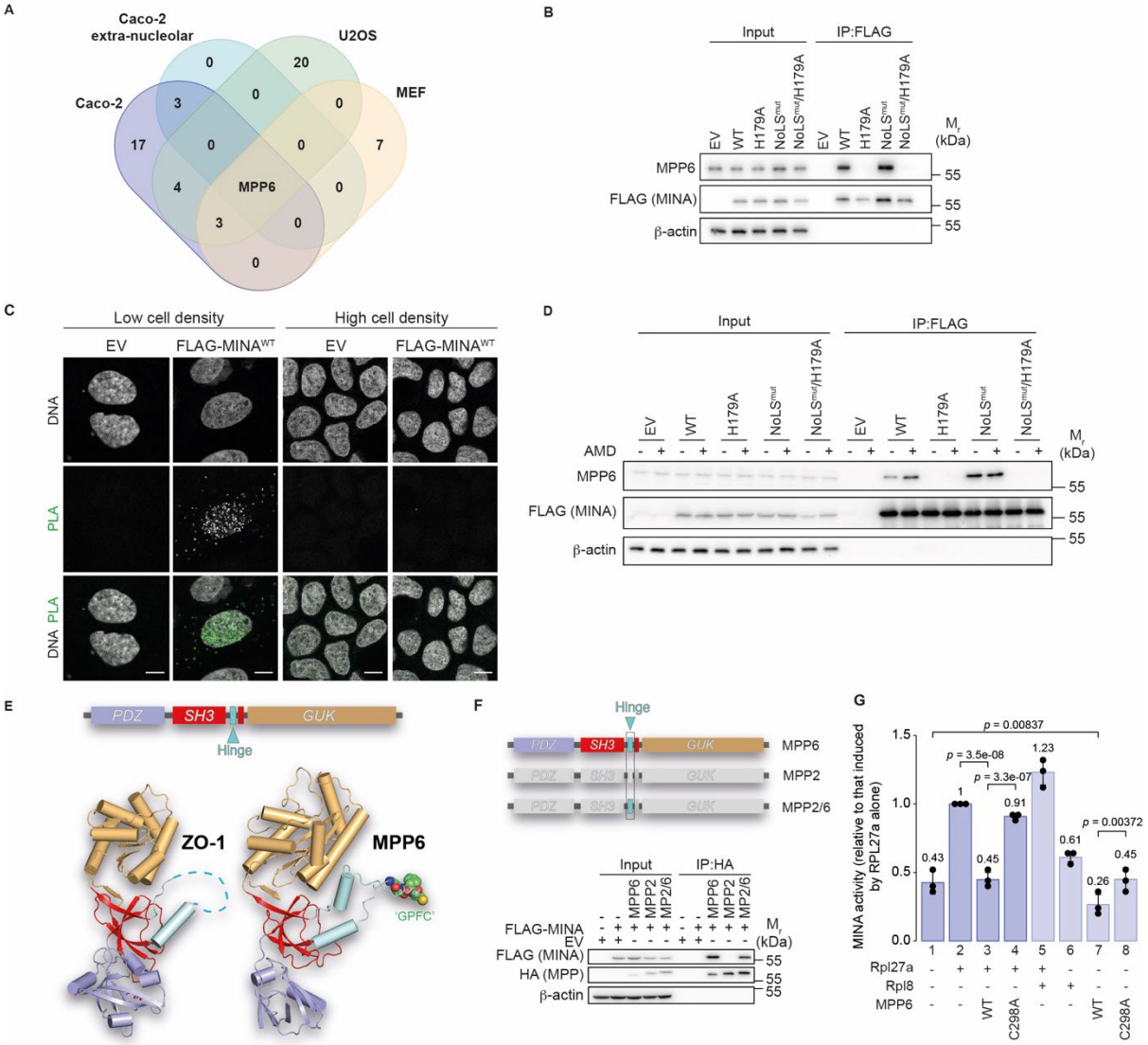

Figure 4. Extra-nucleolar MINA interacts with MPP6, a member of the 'membrane-associated guanylate kinase' (MAGUK) family

(A) *Venn diagram showing the overlap between high stringency MINA-interactomes identified in Caco-2, U2OS and MEF cells. Note that the only common factor that was also upregulated with extra-nucleolar MINA (NoLS^{mut}) was MPP6.*

(B) *Validation of proteomic data. Anti-FLAG immunoprecipitates (IP) from extracts of stable Caco-2 cells expressing the indicated doxycycline-inducible 3xFLAG-MINA constructs were immunoblotted for endogenous MPP6 (61 kDa), FLAG (MINA, 53 kDa). For MPP6 the input is 0.6% of the IP, for FLAG and β-actin it is 31%.*

(C) *Proximity ligation assays (PLA, green foci) indicate that MINA and MPP6 preferentially interact in the nuclei (gray) of subconfluent Caco-2 cells. Scale bars, 10 µm.*

(D) *The interaction of MPP6 with MINA is suppressed by RNA polymerase I activity. Anti-FLAG IPs from extracts of stable SW620 cells expressing an empty vector (EV) or the indicated 3xFLAG-MINA constructs were immunoblotted for MPP6 (61 kDa) and FLAG (MINA, 53 kDa). Expression of 3xFLAG-MINA was induced with 0.2 µg/mL doxycycline for 24 h before the cells were treated with 40 ng/mL actinomycin D (AMD) for 4 h. Input = 1%.*

348 ***(E)*** *MPP6 domain architecture. Top, Cartoon representation of the 'PSG' supramodule.*
349 *Bottom, Comparison of the X-ray structure of the PDZ-SH3-GUK region from a canonical*
350 *MAGUK protein ZO-1 (PDBID:3SHW) and the predicted structure of the equivalent region of*
351 *MPP6 generated with AlphaFold. The GPFCG motif is highlighted in space-filling*
352 *representation and is located at the tip of the unstructured 'Hinge' insert. The yellow ball*
353 *represents residue C298.*
354 ***(F)*** *The Hinge domain of MPP6 is sufficient for MINA binding. An MPP2 chimera that contains*
355 *the Hinge domain of MPP6 (AAs 285-338) ('MPP2/6'), but not wildtype MPP2, coprecipitates*
356 *FLAG-MINA. Top, Graphical representation of the constructs used in the bottom panel.*
357 *Bottom, Anti-HA immunoprecipitates from extracts of HEK293T cells expressing the indicated*
358 *constructs were immunoblotted as indicated. For FLAG and β-actin the input is 10% of the IP,*
359 *for HA it is 20%.*
360 ***(G)*** *An MPP6 peptide containing the minimal determinants for MINA binding*
361 *(SQFLEEKRKAFVRRDWDNS**GPFCG**TISSKKKKK) blocks RPL27A peptide*
362 *(GRGNAGGL**H**HHRINFDKYHP)-induced MINA activity in vitro. An NO66 substrate peptide*
363 *(Rpl8; NPVEHPFGGGNHQHIGKPSTI), which is known not to support MINA activity [13] was*
364 *used as negative control. MINA activity was determined using an indirect coupled assay based*
365 *on succinate production (see STAR Methods). Bars represent the average of n = 3 biological*
366 *repeats. Averages are indicated above each respective bar. Error bars, SD. Statistical*
367 *significance was determined using a one-way ANOVA and p values were calculated post-hoc*
368 *using a pairwise t test. P values were adjusted using the Benjamini-Hochberg correction for*
369 *multiple comparisons. Uncropped western blot images are presented in source data.*
370
371
372
373 To test the requirements of these MPP6 domains for MINA binding we analyzed a series of
374 MPP6 truncation mutants in immunoprecipitation and immunofluorescence experiments
375 (Figures S8A, S8B, and S8C). The results suggest that the minimal MPP6 domain required
376 for MINA binding is within the non-canonical SH3 domain, i.e. amino acids 285-338, which
377 contains the so-called Hinge domain (Figures 4E and S8B). To test whether this domain is
378 sufficient for MINA binding we created an MPP2/6 chimera by swapping the Hinge domain of
379 MPP2 (which does not bind MINA; Figure S7D) with the corresponding domain of MPP6
380 (Figure 4F, top). Immunoprecipitation analysis confirmed that the MPP6 Hinge domain is
381 sufficient for MINA binding in this context (Figure 4F, bottom). To further narrow down the
382 binding determinants, we next focused on the differences in primary sequence between MPP2
383 and MPP6 in this region. The sequence identity of this region is 67.9%, suggesting that the
384 strikingly different MINA binding profiles are determined by the relatively few regions of low
385 homology (Figure S8D). To test the importance of these regions we swapped residues within
386 them in the context of the MPP2/6 chimera. A small insertion at the N-terminal end of the
387 MPP2 Hinge domain was sufficient to prevent MINA binding (Figure S8E). Next, we alanine
388 scanned residues 287-303 within the Hinge domain of full-length MPP6 and identified residues
389 295-299 (sequence GPFCG) as critically required for MINA binding (Figure S8F). These

390 residues are situated at the predicted apex of the unstructured and solvent-exposed loop of
391 the Hinge domain (Figure 4E), and are therefore likely to be available for protein:protein
392 interactions. Together, these data are consistent with a site-specific interaction of MINA with
393 a minimal sequence motif within the Hinge domain of MPP6.
394
395 **The Hinge region of MPP6 mediates a pseudo-substrate-like interaction with MINA**
396 MINA interacts with MPP6 in an activity-dependent manner (Figures 4B, 4D, S7A and S7B).
397 The interaction of MINA with the MPP6 Hinge domain retains its dependence on MINA
398 hydroxylase activity (Figures S8G and S8H). Activity-dependence of binding can be an
399 indicator that a hydroxylase interactor is a novel substrate[28,29]. Therefore, we next explored
400 whether MPP6 is hydroxylated by MINA.
401
402 MPP6-3xFLAG was overexpressed in the presence or absence of HA-MINA before
403 immunoprecipitation (Figure S9A), in-solution chymotrypsin digest, and LC-MS/MS analysis.
404 Near complete (98%) peptide-level sequence coverage of MPP6 was achieved in database
405 searches that also considered a wide-range of residue-specific oxidations (Figure S9B).
406 Consistent with the lack of homology between the known substrate RPL27A and the Hinge
407 domain of MPP6 (Figure S9C) we did not detect histidyl hydroxylation in this region. Oxidized
408 peptides encompassing the Hinge domain were detected that could be confidently assigned
409 to W291 (Figures S9D and S9E). However, the stoichiometry was low and did not respond to
410 MINA overexpression (Figure S9F). Neither subconfluent culture (where MINA binding is
411 predicted to increase), or proteasomal inhibition, led to elevated W291 oxidation, even in the
412 presence of MINA overexpression (Figure S9F). We note that tryptophan can undergo
413 spontaneous chemical oxidation as an artefact of sample preparation for MS[30-32].
414
415 In order to take an orthogonal approach that avoids the limitations of mass spectrometry
416 analysis and artefactual oxidation we next used a coupled in vitro enzyme assay. Although
417 the currently assigned hydroxylase activity of MINA is restricted to histidyl residues, we noted
418 the absence of a histidine in the minimal domain within MPP6 that is required for MINA binding
419 (residues 295-299). Since some closely related JmjC-hydroxylases can target multiple amino
420 acid types[33-36], we first explored the potential for wider biochemical specificity of MINA,
421 including the amino acids in this region of MPP6 (Gly, Pro, Phe, and Cys). To do this we used
422 RPL27A peptides with the corresponding amino acid substitutions at the H39 target residue:
423 Unlike the wildtype RPL27A peptide sequence, neither H39G, H39P, H38F or H39C peptides
424 were able to support MINA activity (Figure S10A). Similar data were obtained using H39W-,
425 H39S-, H39N-, H39D-, H39K-, and H39R-substituted peptides. These data indicate that MINA

426 does not have a broad biochemical activity and is unlikely to hydroxylate residues found within
427 the MPP6 minimal binding domain. To explore this directly, we tested three MPP6 peptides of
428 varying length and position that overlap the GPFCG motif and wider Hinge region of MPP6
429 (which is sufficient for activity-dependent MINA binding, Figure 4F) (Figure S10B). Unlike the
430 RPL27A peptide, none of the MPP6 peptides supported MINA activity (Figure S10C).
431
432 Overall, therefore, our cell-based and in vitro studies did not identify a MINA-dependent
433 hydroxylation of MPP6. We cannot rule out the presence of a modification that was below the
434 limits of detection, the catalysis of a previously undescribed oxidative modification, or
435 subsequent processing of an oxidized species. However, it is also possible that, unlike the
436 activity-dependent interactions of related JmjC hydroxylases that led to novel substrate
437 assignments[28,29], the activity-dependent interaction described here is unique. For example,
438 the interaction of MPP6 with MINA may require the integrity and availability of the catalytic
439 pocket, rather than being 'activity-dependent' per se. In line with MPP6 binding directly to the
440 MINA catalytic pocket, an MPP6 peptide containing the GPFCG motif prevented RPL27A-
441 induced MINA activity (Figure 4G; compare 2nd and 3rd bar) and significantly reduced its
442 'uncoupled' turnover (compare 1st and 7th bar). Both effects were specific as they were not
443 observed with a control peptide (NO66 substrate Rpl8) (compare 2nd, 3rd, and 5th bars, and 1st,
444 6th and 7th bars). Furthermore, both effects of the MPP6 peptide were ablated by the C298A
445 substitution (compare 3rd and 4th bar, and 7th and 8th bar) (Figure 4G), which is sufficient to
446 block binding of MPP6 to MINA (Figure S8F). Overall, our data are consistent with the
447 possibility that the solvent exposed C298 residue of the MPP6 Hinge domain binds to the
448 MINA catalytic pocket in a pseudo-substrate-like manner.
449
450 **MINA regulates MPP6 expression and localization**

451 Although we did not identify a modification arising from MINA binding to MPP6, we were
452 intrigued that the function of the interaction might be related to the role of the Hinge domain in
453 other MAGUKs, i.e. membrane localization and protein stability[27,37]. MINA knockdown caused
454 a reduction in membrane staining and increase in nuclear localization of MPP6 in low-density
455 cultures (Figures 5A and 5B), in parallel with a reduction in MPP6 protein expression (Figure
456 5C). Consistent with these changes being a direct consequence of the interaction with MINA,
457 a constitutively expressed MPP6 mutant that fails to bind MINA (C298A) was nuclear localized
458 and underexpressed (Figures 5D and 5E). These data suggest that the interaction of MINA
459 with MPP6 in the nucleus (Figures 4C) promotes the subsequent localization of MPP6 to the
460 plasma membrane.

461

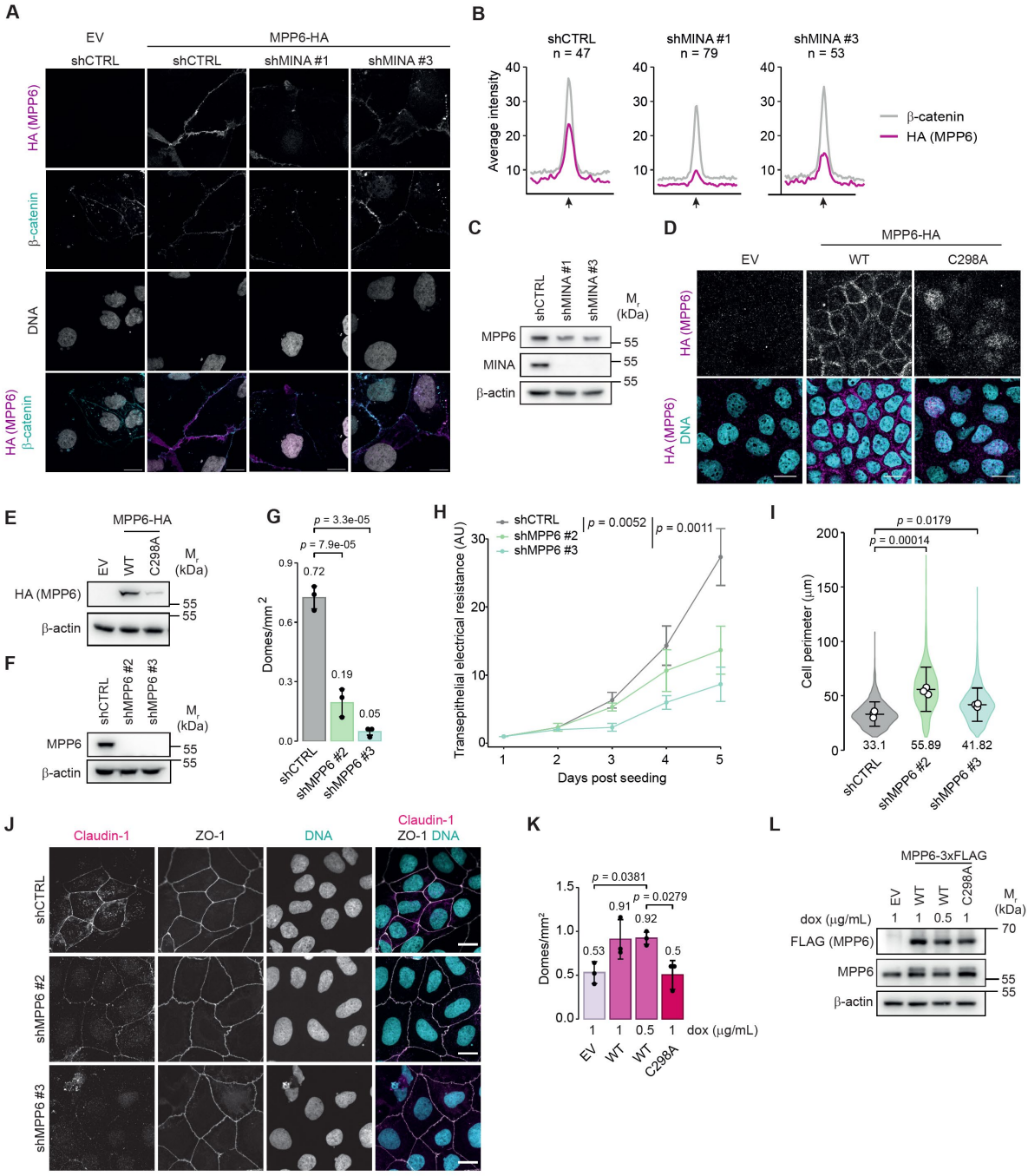

Figure 5. MPP6 promotes tight junction integrity and epithelial barrier function

(A) *MINA depletion reduces membrane localization and increases nuclear distribution of MPP6. Representative immunofluorescence images of subconfluent Caco-2 cells expressing the indicated shRNAs and stained for HA (magenta), β-catenin (cyan) to mark the membranes and DNA (DAPI, gray). Scale bars, 20 µm.*

(B) *Reduced membrane staining of MPP6-HA in MINA-depleted cells under conditions presented in (A). Line graphs indicate the average fluorescence intensity of a line drawn across the membrane connecting two cells, measured with Fiji. The average of n = 3 biological experiments is shown. The total number of images analyzed for each condition is shown above each respective graph. β-catenin was used as membrane marker.*

474 ***(C)*** *MINA depletion reduced MPP6 expression in subconfluent Caco-2 cultures. Whole cell*
475 *extracts from cells expressing the indicated shRNAs were immunoblotted for MPP6 (61 kDa)*
476 *and MINA (53 kDa).*
477 ***(D)*** *Altered localization of HA-tagged MINA-binding mutant MPP6^{C298A}. Stable Caco-2 cell*
478 *lines constitutively expressing an empty vector (EV), wildtype (WT) or MPP6-HA C298A were*
479 *stained for HA (MPP6, cyan) and DNA (DAPI, cyan). Scale bars, 20 µm.*
480 ***(E)*** *Reduced expression of HA-tagged MINA-binding mutant MPP6^{C298A}. Whole cell extracts*
481 *were immunoblotted for HA (MPP6, 61 kDa).*
482 ***(F)*** *Representative immunoblot from whole cell extracts of stable Caco-2 cells expressing the*
483 *indicated shRNAs showing efficient depletion of MPP6 (61 kDa).*
484 ***(G)*** *MPP6 depletion reduces dome formation. Bar graph showing the average number of*
485 *domes per mm^2 of n = 3 independent experiments. The average of each condition is shown*
486 *above each respective bar.*
487 ***(H)*** *Delayed establishment of transepithelial electrical resistance in MPP6-depleted cells. Line*
488 *graph depicts the average of three technical repeats of one biological repeat. The experiment*
489 *was repeated 4 times with similar results. Statistical significance was determined on day 5.*
490 ***(I)*** *Increased perimeter of cells in MPP6-depleted monolayers. Violin plot represents the data*
491 *from n = 3 experiments. Average of each condition is shown underneath each respective violin.*
492 *n = 2612 (shCTRL), n = 1450 (shMPP6 #2) and n = 1958 (shMPP6 #3) cells were quantified.*
493 ***(J)*** *Altered localization of Claudin-1 following MPP6 knockdown. Representative images of*
494 *Caco-2 monolayers expressing the indicated shRNAs were stained for Claudin-1 (magenta),*
495 *ZO-1 (gray) and DNA (DAPI; cyan). Scale bars, 20 µm.*
496 ***(K)*** *MPP6-induced dome formation is dependent on C298. Expression of wildtype (WT) or*
497 *MINA-binding mutant C298A MPP6-3xFLAG were induced with doxycycline (dox) at the*
498 *indicated concentrations. Note that a reduced concentration of dox (0.5 µg/mL) was included*
499 *for WT to allow fair comparison to the reduced expression levels observed for C298A (as also*
500 *presented in (E)). Domes were counted 4 days post seeding.*
501 ***(L)*** *Cell extracts of samples treated as in (K) were immunoblotted for FLAG (MPP6) and MPP6*
502 *(61 kDa).*
503 *(G-I and K) Statistical significance was determined using a one-way ANOVA and p values*
504 *were calculated post-hoc using a Dunnett's multiple comparisons test. Error bars, SD.*
505 *(C, E, F and L) β-actin (42 kDa) was used as loading control. Uncropped western blot images*
506 *are presented in source data.*
507

508

509 **MPP6 is required for the timely establishment of cell-cell junctions**

510 Considering the effect of MINA knockdown on barrier function (Figure 1) and MPP6 membrane
511 localization and expression (Figures 5A and 5B), we hypothesized that MPP6 knockdown
512 would phenocopy MINA loss of function. Indeed, shRNA knockdown of MPP6 severely
513 impaired dome formation and TEER (Figures 5F, 5G and 5H) and increased the length of the
514 cell perimeter (Figures 5I), with concomitant reduction in membrane staining and expression
515 of Claudin-1 (Figures 5J, S11A and S11B). Similar to MINA knockdown, this occurred in the
516 absence of gross changes in cell proliferation (Figure S11C). To explore the effect of the MPP6

517 C298A mutant we switched to a tunable doxycycline-inducible system, due to the known
518 confounding effects of overexpressing membrane/polarity proteins in some circumstances,
519 and the differential expression of constitutively expressed wildtype and C298A MPP6 (Figure
520 5E). Using this system, we observed that modest expression of MPP6-3xFLAG was sufficient
521 to promote dome formation (Figures 5K and 5L). The MPP6 C298A mutant, which impairs
522 MINA binding, was completely inactive in this regard (Figure 5K and 5L).
523

524 **The MINA-MPP6 pathway is required for normal 3D growth and morphogenesis**

525 To investigate the importance of the MINA-MPP6 pathway in 3D growth and tissue
526 morphogenesis, Caco-2 cells expressing doxycycline-induced control, MINA or MPP6 shRNA
527 were seeded as single cells in Matrigel and grown for 7 days to form polarized spheroids with
528 a fluid-filled lumen[17]. Depletion of MINA or MPP6 was sufficient to interfere with spheroid
529 morphology including lumenogenesis (Figures 6A,B and S12A,B), size (Figure 6C,D), and
530 growth (Figure 6E,F). Immunofluorescence analysis revealed a diffuse staining pattern of
531 Claudin-1 and ZO-1 and altered nuclear morphology (Figure 6G,H). Although these
532 observations may be consistent with some level of defective polarity, a luminal surface was
533 still largely maintained in these spheroids (Figure 6G,H). Consistent with the 2D data
534 presented above, MINA and MPP6 depletion also reduced Claudin-1 levels (Figure S12C,D).
535 Expression of the MINA binding defective MPP6 mutant (C298A) phenocopied MINA and
536 MPP6 loss of function, causing reduced lumenogenesis, decreased spheroid size, and diffuse
537 localization of ZO-1 (Figure 6I).
538

539 Overall, our data are consistent with MPP6 acting in a pathway downstream of extra-nucleolar
540 MINA that regulates cell adhesion, barrier function, and morphogenesis. Because this
541 pathway is suppressed by RNApol1 activity and the nucleolar proteome, the work identifies a
542 novel link between ribosome biogenesis and epithelial membrane biology.
543

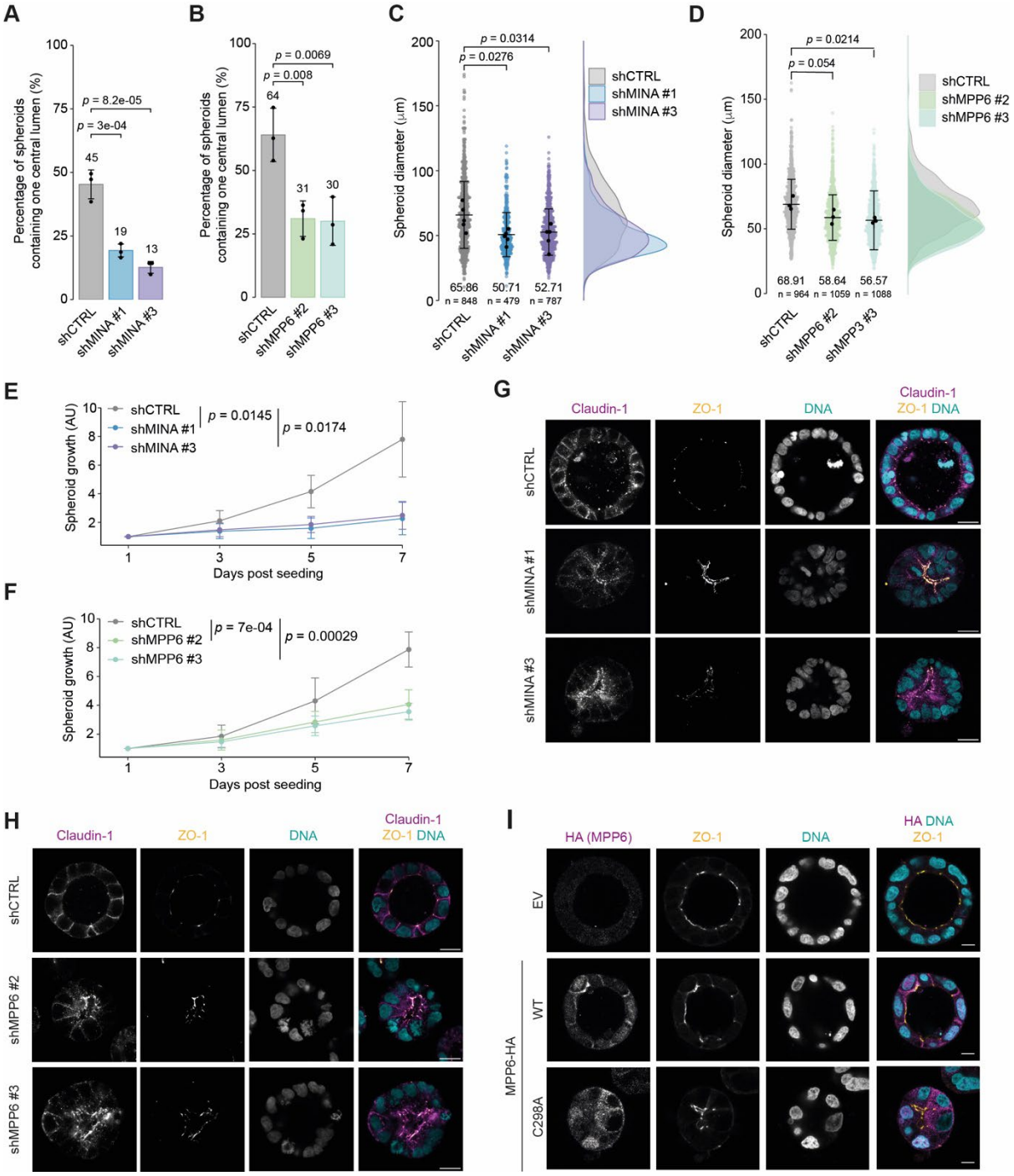

Figure 6. The MINA-MPP6 pathway is required for spheroid lumenogenesis, growth and polarity.

(A and B) *Quantification of lumen formation in spheroids grown from stable Caco-2 cells expressing the indicated MINA (A) or MPP6 (B) shRNA sequences. Bars represent the average percentage of spheroids with one central lumen of n = 5 (C) and n = 3 (D) independent experiments. The average of each condition is shown above each respective bar.*

(C and D) *Quantification of size of spheroids grown from stable Caco-2 cells expressing the indicated MINA (C) or MPP6 (D) shRNA sequences. Horizontal lines represent the average spheroid diameter from n = 3 independent experiments. The average of each condition and the number of spheroids counted are shown below each respective beeswarm.*

555 ***(E and F)*** *MINA (E) and MPP6 (F) depletion reduces spheroid growth. Growth of spheroids*
556 *was analyzed using a CellTiter-Glo Luminescent Cell Viability Assay kit after 3, 5 and 7 days*
557 *in culture. Presented values are the average of n = 4 independent experiments. AU, arbitrary*
558 *unit.*
559 ***(G and H)*** *MINA (G) and MPP6 (H) depletion prevent appropriate membrane localization of*
560 *Claudin-1 and ZO-1. Representative immunofluorescence images of 3D Caco-2 spheroids*
561 *expressing the indicated shRNAs and stained for Claudin-1 (magenta), ZO-1 (yellow), and*
562 *DNA (DAPI, cyan). Scale bars, 20 µm.*
563 ***(I)*** *MPP6 C298A overexpression phenocopies MINA and MPP6 knockdown. Single cells were*
564 *grown to spheroids for 7 days, fixed and stained for HA (MPP6, magenta) and tight junction*
565 *marker ZO-1 (yellow). Nuclei were visualized with DAPI (cyan). Scale bars represent 10 µm.*
566 ***(A – D)*** *Statistical significance was determined using a one-way ANOVA and p values were*
567 *calculated post-hoc using a Dunnett's multiple comparisons test. Error bars, SD.*
568
569
570
571

572 ## Discussion

573 Here in this paper, we have uncovered the extra-nucleolar function of the protein hydroxylase
574 MINA, demonstrating, for the first time, that it controls epithelial TJ integrity, barrier function,
575 and morphogenesis through its interaction with the MAGUK protein MPP6. In doing so we
576 have discovered that cellular growth status and ribosome biogenesis are functionally coupled
577 to the epithelial plasma membrane, via a novel nuclear partnership between MPP6 and the
578 2OG-oxygenase MINA. The work raises the intriguing possibility that ribosome biogenesis
579 might also couple to membrane biology in other ways, and that other growth responsive
580 cellular processes might sink proteins that would otherwise suppress such roles. Could the
581 uniquely nutrient-dependent 2OG-oxygenase family play a more general role in signaling
582 between subcellular compartments to couple cell systems controlling cell growth and
583 differentiation?
584
585 Although 2OG-oxygenases are still considered an emerging enzyme family, relative to others
586 (such as kinases), they have already been implicated in a variety of essential cellular systems,
587 from oxygen sensing and epigenetics to protein translation and collagen synthesis[38,39]. These
588 enzymes have not previously been demonstrated to play a role in regulating cell polarity and
589 adhesion through the direct interaction with peripheral membrane proteins, however. Although
590 the interaction with MPP6 was entirely dependent on the integrity of a critical Fe(II)-binding
591 residue within the MINA catalytic pocket (Figure 4), it did not result in a detectable
592 hydroxylation event (Figures S9 and S10). Although more work is required to definitively
593 conclude that a modification is not catalyzed, it is also possible that MPP6 is sensing the

594 availability of the catalytic pocket as an indicator of the absence of RPL27A and/or co-factors.
595 Indeed, computational investigation of potential MPP6 interaction modes suggests that the
596 GPFCG region at the tip of the Hinge domain (Figures 4E and S8F) might directly bind the
597 MINA active site through formation of β-turn like structures (Figure S13). Although 'pseudo-
598 substrates' have been identified for other enzyme classes, this may be one of the first potential
599 candidates that we know of for the 2OG-oxygenase family. As such, the work is relevant to
600 the wider field: Protein hydroxylases, including Hypoxia Inducible Factor prolyl hydroxylases,
601 may be at risk of substrate misassignment[31], in part because of the artefactual oxidation of
602 residues such as tryptophan during MS sample preparation, as also demonstrated here
603 (Figure S9). Our work raises the possibility that some proteins that interact with the catalytic
604 domain of 2OG-oxygenases may be doing so in a pseudo-substrate-like manner, rather than
605 as prime substrates.
606
607 Through our phenotypic and proteomic analyses of MINA, we have helped clarify the function
608 of the poorly characterized human MAGUK protein MPP6. The *drosophila* homologue of
609 MPP6 (*Varicose*) has been more extensively studied than its human counterpart: *Varicose* is
610 essential for the assembly and function of septate junctions (which are thought to be the
611 equivalent of vertebrate TJs) and for normal tracheal development[40,41]. A similar role for MPP6
612 in TJ function in human cells is supported by our results showing that its loss of function causes
613 reduced dome and TEER formation and decreased Claudin-1 expression (Figure 5). Under
614 conditions of MINA or MPP6 knockdown we did not observe widespread mis-localization of
615 tight or adherens junction markers however, particularly in 2D. Similar observations were
616 made with *Varicose*[40] and with other human polarity proteins, including MPP7, Scribble and
617 Par3[42-44]. The prevailing hypothesis is that such proteins are not primarily involved in the
618 establishment of apico-basal cell polarity, but rather in ensuring and maintaining junctional
619 functionality. MINA appears to promote this function at least in part by facilitating MPP6
620 membrane localization (Figures 5A and 5B), which could in turn support normal expression
621 (Figure 5C), as observed for other peripheral membrane proteins[32]. How MINA achieves this
622 is not yet clear, although it seems likely that this is a consequence of the direct interaction with
623 the Hinge domain of MPP6 in the nucleus. Although the function and interacting partners of
624 the MPP6 Hinge domain are poorly characterized, mutagenesis screens in the fly model
625 demonstrate it is essential[40]. The Hinge domain of related human MAGUK proteins have been
626 implicated in membrane localization, protein-protein interactions, and proteasomal
627 degradation[27,37], consistent with the results described here. Further work is required to explore
628 how extra-nucleolar MINA supports the translocation of nuclear MPP6 to the plasma
629 membrane to function in TJ biology.
630

631 TJs are critical for normal physiology and have been heavily implicated in disease[45-47]. Their
632 barrier function plays a critical role in regulating permeability to small molecules, immune cells,
633 pathogens, and parasites, and as such has been implicated in a wide variety of diseases
634 across multiple tissues, including colitis, infection, edema, and allergy[45-47]. In light of the results
635 presented here, it will be of interest to study the role of the MINA-MPP6 pathway in these
636 contexts. A single-nucleotide polymorphism in the MINA gene is associated with increased
637 risk of asthma in children[48], and MINA knockout reduces the allergic response to inhaled
638 allergens in mice[49]. MINA knockout mice also show increased clearance of parasitic
639 gastrointestinal nematode worms[50], which in some contexts can be associated with increased
640 barrier permeability that supports the 'washer/sweeper' effect and/or immunological
641 access[51,52]. Whether a deregulated MPP6-TJ pathway could play a role in these contexts is of
642 interest and warrants future investigation.
643
644 Alterations in cell:cell junctions and adhesion is a hallmark of cancer[53]. Loss of tumor
645 suppressor genes in TJ complexes and signaling pathways disrupts their fence function,
646 resulting in abnormal polarity and reduced cell:cell adhesion, which together disrupt
647 morphogenesis and promote migration/invasion[54]. Although several mechanisms have been
648 described by which TJs are rendered dysfunctional in epithelial cancers, it is likely that others
649 remain to be discovered: We propose that the MINA-MPP6 pathway is one such candidate
650 that is worthy of further investigation, for the following reasons. Firstly, although MINA has
651 been proposed as a biomarker and drug target in a range of tumor types (reviewed in[55]), there
652 is emerging evidence supporting a paradoxical and poorly characterized role in tumor
653 suppression[15,16]. Secondly, low MPP6 expression is associated with poor prognosis in some
654 cancers, and the MPP6 gene is located in a chromosomal region (7p15-21) altered in several
655 tumor types[56-63]. Thirdly, MPP6 interacts with Cell Adhesion Molecule 1 (CADM1), an
656 immunoglobulin superfamily transmembrane protein that is a tumor suppressor in a wide
657 variety of cancers[64]. Importantly, CADM1 loss-of-function is associated with reduced Claudin-
658 1 expression and barrier function[65,66], which phenocopies MINA and MPP6 knockdown
659 (Figures 1 and 5). Future work should focus on the mechanisms by which the MINA-MPP6
660 pathway may be inactivated in cancer and the consequences of this on the barrier and fence
661 functions of TJs. Furthermore, the work presented here suggests that an important mechanism
662 by which the MINA-MPP6 pathway could be suppressed is through oncogene-induced
663 nucleolar sequestration of MINA due to elevated RNAPol1 activity and ribosome biogenesis.
664 RNAPol1 inhibitors are being considered as novel chemotherapeutics (reviewed in[67]): Our
665 hypothesis would predict that such treatments might not only negatively impact growth and
666 viability, but also help to 'normalize' cell:cell adhesion and polarity in some contexts.
667

668 ## Methods

669 ### Plasmid constructs and cloning procedures

670 Coding sequences of MINA, MPP6 and NO66 were PCR cloned from plasmid DNA or cDNA
671 into pFLAG (Sigma), pEF6 (Invitrogen), pTIPZ, pIPZ or pIHZ vectors. pIPZ and pTIPZ are
672 derivatives of the pGIPZ and pTRIPZ lentiviral vectors (Open Biosystems) that lack green
673 fluorescent protein (GFP) and red fluorescent protein (RFP), respectively. The coding
674 sequences of MPP2 and MPP2/6 hybrids containing C-terminal HA-tags and restriction sites
675 required for cloning into the pIPZ vector were obtained from Thermo Scientific as GeneArt
676 String Fragment. Non-targeting control (ULTRA-NT#4), MINA (ULTRA-3406274, ULTRA-
677 3406273) and MPP6 (ULTRA-3337606, ULTRA-3337607) shRNA sequences in pZIP-TRE3G
678 vectors were obtained from TransOMIC. PCR reactions were driven by the Phusion High
679 Fidelity DNA polymerase (New England Biolabs (NEB), M0530). Primers were designed to
680 contain a C- or N-terminal tag and the required restriction sites for subsequent ligations.
681 Constructs were confirmed by sequencing, carried out by Source Bioscience. For nucleotide
682 exchanges, site-directed mutagenesis was performed using a Phusion Site-directed
683 Mutagenesis kit (Thermo, F541). 5' termini of the primers were phosphorylated using T4
684 polynucleotide kinase (PNK, Thermo, EK0031) prior to the reactions. All constructs were
685 confirmed by sequencing.

686

687 ### Cell culture

688 HEK293T, Caco-2, SW620 and U2OS cells were cultured in Dulbecco's Modified Eagle
689 Medium (DMEM, Gibco) supplemented with 10% (v/v) fetal bovine serum (FBS, Sigma) and
690 100 international units/mL (IU/mL) penicillin and 100 µg/mL streptomycin (Gibco). Cell culture
691 medium for stable cell lines was supplemented with 1 µg/mL puromycin (Gibco). For 3D
692 spheroid cultures, Caco-2 cells were seeded into Matrigel-coated (Corning, 35621) chamber
693 slides and the culturing medium was supplemented with 4% (v/v) Matrigel. All cell lines were
694 grown at 37°C in a humidified atmosphere with 5% (v/v) CO_2. All cell lines were regularly
695 tested for mycoplasma contamination using a LookOut® Mycoplasma PCR Detection kit
696 (Sigma, MP0036).

697 Where doxycycline-inducible shRNA cell lines were used for experiments, shRNA expression
698 was induced using 1 µg/mL doxycycline (Sigma, D9891) for 72 h before seeding.
699 Subsequently, the culturing medium was refreshed, and fresh doxycycline was added every
700 48-72 h.

701

702 **Transient transfection**

703 Plasmid DNA transfections were performed using FuGENE® 6 transfection reagent
704 (Promega). Briefly, the transfections mix was made up in Opti-MEM™ (Gibco, 31985070)
705 using a ratio of DNA to transfection reagent of 1:3 and incubated for 15-30 min at room
706 temperature (RT) before the complexes were added to the cells. 500 ng of DNA was used per
707 mL of culturing medium. Cells were seeded 24 h before transfection and lysed or fixed 48 h
708 after transfection.

709 **Generation of stable cell lines**

710 Stable expression cell lines were generated by transduction with lentivirus. For lentivirus
711 production, HEK293T cells were transfected with the plasmid of interest (50%), the packaging
712 vector psPAX2 (35%) and envelope vector pMD2.G (15%) as described above. The lentivirus-
713 containing supernatant was collected 48 h after transfection, passed through a 0.45 µM
714 polyethersulfone (PES) filter, diluted 1:1 with fresh medium and added to the recipient cells
715 for 48 h. Thereafter, transduced cells were selected using puromycin (2 µg/mL final
716 concentration, Gibco).

717 **Metabolic labelling of newly synthesized proteins**

718 Protein synthesis was monitored with L-azidohomoalanine (AHA) using a Click-iT™ Nascent
719 Protein Synthesis kit (Thermo Scientific) according to the instructions of the manufacturer.
720 Briefly, cells were incubated with methionine-free medium for 1 h before AHA was added at a
721 final concentration of 50 mM. After 1 h, cells were fixed and permeabilized as described below.
722 Next, Alexa Fluor 595 Alkyne diluted in Click-iT® Cell Reaction Buffer (Thermo Scientific) at a
723 final concentration of 2.5 mM was conjugated to any incorporated AHA.

724 **Proximity ligation assay**

725 Duolink® proximity ligation assay kits were purchased from Sigma-Aldrich and performed
726 according to the manufacturer's instructions.

727 **Immunofluorescence staining**

728 For immunofluorescence studies of 2D cultures, cells were grown on poly-D-lysine-coated or
729 uncoated glass coverslips and fixed or 4% (w/v) paraformaldehyde (PFA) for 15 min at RT
730 with methanol for 10 min at -20°C. Where methanol was used, it is stated in the figure caption.
731 Cells fixed with PFA were subsequently permeabilized using 0.1% (v/v) Triton in PBS for 10
732 min at RT. Next, cells were blocked with 1% (w/v) bovine serum albumin (BSA) in PBS for 1
733 h at RT and subsequently incubated overnight (ON) at 4°C with primary antibodies diluted in
734 1% (w/v) BSA in PBS. The following primary antibodies were used: FLAG (Sigma, F1804,
735 1:1,000), HA (Covance, MMS-101P, 1:500), HA (Cell Signaling Technology (CST), C29F4,
736 1:500), nucleolin (Santa Cruz Biotechnology (SCB), sc-13056, 1:200-1:1,000),

737 nucleophosmin-1 (SCB, sc-6013-R, 1:200), MINA (Invitrogen, 39-7300, 1:100), Claudin-1
738 (Abcam, ab211737, 1:500), β-catenin (BD Transduction Laboratories, 610153, 1:500). The
739 next day, coverslips were washed with 1% (w/v) BSA in PBS and incubated with secondary
740 antibodies diluted in 1% (w/v) BSA in PBS for 1 h at RT. Alexa Fluor 488, 555 or 633 secondary
741 antibodies were purchased from Invitrogen and used at a final concentration of 1:1,000. Nuclei
742 were stained by incubation with 0.5 – 1 µg/mL 4',6-diamidino-2-phenylindole (DAPI, D1306,
743 Invitrogen) in PBS for 10 min at RT, and the coverslips were mounted with Prolong Gold
744 antifade mountant (Molecular Probes) onto microscope slides.

745 Caco-2 cells grown as 3D cultures were fixed with 4% (w/v) PFA/5% (w/v) sucrose in PBS for
746 20 min at RT, washed 3 times with PBS and incubated with 100 mM glycine in PBS for 20 min
747 at RT to quench unreacted aldehydes. Subsequent permeabilization, blocking and staining
748 were performed as described above. Stained spheroids were stored in PBS at 4°C until they
749 were imaged.

750

751 **Image acquisition, processing, and quantification**

752 Confocal images were acquired using a Zeiss LSM 780 or 880 laser scanning confocal system
753 equipped with a 20x, 40x or 60 C-Apochromat 1.2 W Korr M27 objective. Immunofluorescence
754 images of similarly stained experiments were acquired with identical laser power and detector
755 gain. Images were processed using Fiji software (https://fiji.sc) and arranged in Adobe
756 Illustrator. Brightness and contrast were adjusted using only linear operations applied to the
757 entire image.

758 Cell perimeters were measured using the CellMorph plugin for Fiji
759 (https://github.com/viboud12/CellMorph). Ten random images were taken for each condition
760 in each experiment. Quantification was based on ZO-1 staining.

761 Phase-contrast images were acquired using an EVOS™ FL color imaging system equipped
762 with a 4x or 10x Plan PH2 objective. To quantify domes, a total of 30 phase-contrast images
763 were taken per condition per experiment, 4 or 5 days after seeding when the cells had formed
764 a confluent monolayer. To quantify spheroids, a total of 10 images were taken per condition
765 per experiment, 7 days after seeding.

766

767 **Multiplex Immunofluorescence Staining**

768 4 µm formalin fixed paraffin embedded (FFPE) normal human colon were sectioned on to
769 TOMO hydrophilic adhesive microscope slides (Matsunami).

770 Following antibody validation, fully automated multiplex immunofluorescent staining was
771 performed on the Ventana Discovery Ultra platform (Roche Tissue Diagnostics, RUO
772 Discovery Universal V21.00.0019). Primary- secondary- antibody pairs were as follows: Ki67
773 (Roche Tissue Diagnostics, 05278384001), OmniMap-anti-Rb HRP (Roche Tissue
774 Diagnostics); pan-CKAE1-AE3 (Leica Biosystems, NCL-L-AE1/3,1:250), OmniMap-anti-Ms
775 HRP (Roche Tissue Diagnostics); MINA (Thermo Fisher, 409500, 1:50), OmniMap-anti-Ms
776 HRP (Roche Tissue Diagnostics); UBF1(Abcam, Ab75781, 1:50), UltraMap-anti-Rb HRP
777 (Roche Tissue Diagnostics). Fluorescent detection was performed using an Opal fluorophore
778 tyramide-based signal amplification system (Akoya Biosystems) with the following
779 combinations. Ki67: Opal 570 (1:200); pan-CKAE1-AE3:Opal 620 (1:100) : MINA:Opal 690
780 (1:200); UBF1:Opal 520 (1:200).

781 A nuclear Hoechst 33342 counterstain (Sigma, 14533, 1:50) was applied to each sample for
782 nuclear detection.

783

784 **Multiplex Immunofluorescence Image acquisition and Analysis**

785 Multispectral whole slide images were acquired on a Vectra Polaris imaging system (Akoya
786 Biosystems) using a 40x objective. Spectral unmixing was performed using a spectral library
787 generated from single fluorescence slides of each protein marker with their assigned
788 fluorophore dye, a DAPI only counterstain slide, and an unstained normal colon tissue section.
789 The resulting images were analyzed using Visiopharm software (version 2022.12.0.12865). A
790 bespoke deep learning algorithm was trained using DAPI, UBF1, and Ki67 features to detect
791 nuclei and nucleoli in the epithelial compartment. Mean pixel intensities for each marker, in
792 addition to X,Y coordinates, were exported for subsequent statistical analysis.

793

794 Single cell measures obtained from Visiopharm were analysed using R (version 4.2.2) with
795 tidyverse packages (version 2.0.0). Per crypt binned quartile cellular distances were
796 determined by calculating their perpendicular point along the crypt axis. Nucleolus:Nuclear
797 ratio calculated as mean nucleolar per pixel intensity divided by mean nucleoplasm per pixel
798 intensity.

799

800 **Transepithelial electrical resistance measurements**

801 Caco-2 cells were seeded onto cellQART® permeable support inserts (0.4 mm pore size).
802 The transepithelial electrical resistance (TEER) was measured using an EVOM2 epithelial
803 voltohmmeter (World Precision Instruments, Inc.) and a STX2 electrode (World Precision
804 Instruments, Inc.) according to the manufacturer's instructions. Background resistance was

805 measured using cell-free inserts. Three measurements were taken for each sample at each
806 time point.

807 **Whole cell extracts**

808 Cells were washed and harvested in ice-cold PBS, pelleted by centrifugation at 234 x g and
809 lysed by rotation at 4°C for 1 h in JIES buffer (100 mM NaCl, 20 mM Tris-HCl [pH 7.4], 5 mM
810 MgCl2, 0.5% (v/v) NP-40) containing 1x SIGMAFAST protease inhibitor cocktail (Sigma-
811 Aldrich, S8830). Subsequently, cell debris was pelleted by centrifugation (10 min at 21,910 x
812 g at 4°C) and the supernatant was collected. Protein concentration was determined using
813 Pierce™ 660nm Protein Assay Reagent according to the manufacturer's instructions (Thermo,
814 22660). Finally, protein samples were prepared at equal concentrations in 1x Laemmli Loading
815 Buffer (6x: 125 mM Tris-HCl [pH 6.8], 6% (w/v) SDS, 50% (v/v) glycerol, 225 mM dithiotheitol
816 (DTT), 0.1% (w/v) bromophenol blue) and boiled for 5 min. 3D cell cultures were harvested in
817 ice-cold PBS containing 1x SIGMAFAST protease inhibitor cocktail, pelleted by centrifugation
818 at 21,910 x g at 4°C and washed 3 times with PBS containing 1x SIGMAFAST protease
819 inhibitor cocktail to remove the Matrigel. Subsequently, the cell pellets were resuspended in
820 1x Laemmli Loading Buffer, boiled for 5 min and sonicated.

821 **Immunoprecipitation**

822 For immunoprecipitations, cells were harvested on ice and lysed by rotation for 1 h at 4°C in
823 JIES buffer (see above) containing 1x SIGMAFAST protease inhibitor cocktail (Sigma-Aldrich,
824 S8830). Subsequently, cell debris was pelleted by centrifugation (10 min at 21,910 x g at 4°C)
825 and the supernatant was incubated with anti-FLAG® M2 Magnetic Beads (Sigma-Aldrich,
826 M8823) or anti-hemagglutinin (HA) agarose beads (Sigma-Aldrich, A2095) overnight at 4°C.
827 The next day, beads were washed 6 times with JIES buffer before the immunoprecipitates
828 were boiled for 5 min in 1x Laemmli Loading Buffer or eluted using 100 µg/mL HA (Thermo
829 Scientific, 26184) or 40 ng/mL FLAG (Generon, A6001) peptide in JIES for 15 min at 1,400
830 rpm at RT.

831 **SDS-PAGE and immunoblot analysis**

832 Protein lysates were resolved by sodium dodecyl-sulfate polyacrylamide gel electrophoresis
833 (SDS-PAGE). Protein samples prepared in Laemmli Loading Buffer (see above) were loaded
834 onto either 10%, 12% or 15% (v/v) polyacrylamide gels made in-house, Novex WedgeWell 8-
835 16% gels (Invitrogen, XP08165BOX) or NuPAGE 4-12% Bis-Tris Midi gels (Invitrogen,
836 WG1403A). Electrophoresis was performed in Tris/Glycine/SDS (National diagnostics) or
837 NuPAGE MOPS SDS (Invitrogen, cat. no. NP0001) running buffer. Following SDS-PAGE, the
838 samples were electroblotted onto methanol-activated Amersham Hybond P0.45
839 polyvinylidene difluoride (PVDF) membranes (GE Healthcare) in Tris/Glycine transfer buffer

840 (National diagnostics). Following transfer, the membrane was blocked with 5% (w/v) milk
841 powder dissolved in PBS/0.1% (v/v) Tween-20 (PBS-T) and incubated with primary antibody
842 for 1 h at RT or overnight at 4°C. Where unconjugated primary antibodies were used,
843 immunoblots were subsequently incubated with horseradish peroxidase (HRP)-conjugated
844 secondary antibodies purchased from Cell Signaling. Signals were visualized using Clarity
845 Western ECL reagent (Bio-Rad) or Femto (Thermo Scientific) using a Vilber Fusion Fx. The
846 following primary antibodies were used: FLAG-HRP (Sigma, A8592, 1:10,000), β-actin-HRP
847 (Abcam, ab49900, 1:25,000), HA-HRP (Roche, 12013819001, 1:1,000-1:5,000), MPP6 (Atlas
848 antibodies, HPA019085, 1:500), RPL27A (Abcam, ab74731, 1:500), LIN7C (Proteintech,
849 14656-1-AP, 1:1000), MINA (DSHB, 6C6, 1:40), Claudin-1 (Abcam, ab211737, 1:1000).

850 **Mass spectrometry**

851 MPP6-3xFLAG was anti-FLAG immunopurified from overexpressing HEK293T cells and
852 eluted with 3XFLAG peptide, as outlined above. Samples were extracted, in-solution digested
853 with chymotrypsin, desalted, and analyzed by mass spectrometry as described previously [29].
854 Data were searched against the UniProt Reference Homo sapiens database with PEAKS
855 Studio X Software (Bioinformatics Solutions). Cysteine carbamidomethylation was selected
856 as a 'fixed' modification, with oxidation (M), deamidation (N, Q) and hydroxylation (P, K, D, N,
857 R, Y, H, W) as variable modifications. The data were then filtered to remove methionine
858 oxidations and those with an A-score of <20 (an A-score of 20 corresponds to a modification
859 correctly localized with 99% certainty).

860 ***In vitro* hydroxylation assays**

861 For *in vitro* hydroxylation assays, HA-tagged MINA was overexpressed and purified from
862 HEK293T cells, as described above. Following immunoprecipitation, the purified protein was
863 eluted using 2 µg/mL HA peptide (Thermo Scientific, 26184) in 50 mM HEPES, 50 mM NaCl.
864 Purified enzyme was then incubated with RPL27A peptide (GRGNAGGLHHHINFDKYHP) at
865 a final concentration of 100 µM in 50 mM Tris [pH 7.5], 150 mM NaCl, 1 mM DTT for 5 min at
866 37°C in the presence of 200 µM 2OG, 100 µM Fe(II) and 100 µM ascorbate (final volume 20
867 µL). For peptide competition assays HA-MINA was incubated with a combination of 50 µM of
868 RPL27A peptide and 50 µM of Rpl8 peptide (NPVEHPFGGGNHQHIGKPSTI) or 50 µM of
869 MPP6 peptide (SQFLEEKRKAFVRRDWDNSGPFCGTISSKKKKK) and incubated for 30 min
870 at 37°C. Thereafter, the reaction was quenched with 10 µL of 1% (v/v) formic acid (HCOOH)
871 in H_2O. The presence of hydroxylation was subsequently analyzed using a Succinate-Glo
872 JmjC Demethylase/Hydroxylase Assay kit (Promega), as follows. Samples were diluted 1:10
873 in H_2O and 5 µL of the diluted reaction was mixed with an equal volume of Succinate-Glo
874 detection reagent 1 and incubated for 1 h at RT in a clear bottom 384-well plate. Each reaction

875 was performed in triplicate. Subsequently, 10 µL of Succinate-Glo detection reagent 2 was
876 added, mixed and incubated for 10 min at RT, before luminescence was analyzed.

877 **Structural analysis**

878 Molecular modelling and structural comparisons were carried out using the SSM superposition
879 facility [68] in Coot [69] and visualized in PyMOL (The PyMOL Molecular Graphics System, Version
880 1.2r3pre, Schrödinger, LLC). Coordinates for human MPP6 full-length were obtained either
881 from the AlphaFold database or generated *ab initio* using the ColabFold server [70].

882 **Statistical analysis**

883 Statistical analyses were performed in R. Statistical significance was determined using
884 unpaired t test or one-way analysis of variance (ANOVA) followed by a Dunnett's test or
885 pairwise t tests with Benjamini-Hochberg correction for multiple comparisons. Differences
886 were considered significant at $p<0.05$. Calculated *p* values are shown in each graph. Sample
887 sizes were chosen empirically. Western blot quantifications were performed with Fiji.

888

889 **Acknowledgements**

890 We thank Marion Schmidt-Zachmann (DKFZ, Heidelberg) for the MINA antibody and Peter
891 Ratcliffe, Matthew Cockman, and Sally Roberts for critical reading of the manuscript. E.H. was
892 supported by a BBSRC-MIBTP award to E.H. and M.L.C (1790845). E.H, R.A. and U.B. were
893 funded by a Cancer Research UK Programme Foundation Award to M.L.C. (C33483/A2567).
894 S.J.S. is supported by a transitional award from the Francis Crick Institute (CR2019/003DK).
895 The work was also supported by an MRC project grant to M.L.C. (MR/N021053/1).

896

897 **Author contributions**

898 E.H. and R.A. designed and performed the cell biology experiments, analyzed the resulting
899 data, and generated the corresponding figures. A.K contributed to generation of data. U.B.,
900 J.R.B. and A.Z. contributed to molecular biology. R.H. and R.F. performed mass spectrometry
901 analysis. L.O.-J., R.P., and I.R.P. performed, analyzed, and interpreted multiplex
902 immunofluorescence under the supervision of J.L.Q.. E.H. and M.L.C wrote the manuscript.
903 M.L.C. co-designed the experiments and directed the project. S.J.S. performed structural
904 analyses. All authors approved the final version of the manuscript.

905

906 **Declaration of interests**

907 The authors declare no competing interests.

908

909 **References**

910 1. Zhu, J., and Thompson, C.B. (2019). Metabolic regulation of cell growth and
911 proliferation. Nat Rev Mol Cell Biol *20*, 436-450. 10.1038/s41580-019-0123-5.
912 2. Pelletier, J., Thomas, G., and Volarević, S. (2018). Ribosome biogenesis in cancer:
913 new players and therapeutic avenues. Nat Rev Cancer *18*, 51-63.
914 10.1038/nrc.2017.104.
915 3. Jones, M.C., Zha, J., and Humphries, M.J. (2019). Connections between the cell cycle,
916 cell adhesion and the cytoskeleton. Philos Trans R Soc Lond B Biol Sci *374*, 20180227.
917 10.1098/rstb.2018.0227.
918 4. van Riggelen, J., Yetil, A., and Felsher, D.W. (2010). MYC as a regulator of ribosome
919 biogenesis and protein synthesis. Nat Rev Cancer *10*, 301-309. 10.1038/nrc2819.
920 5. Arabi, A., Wu, S., Ridderstråle, K., Bierhoff, H., Shiue, C., Fatyol, K., Fahlén, S.,
921 Hydbring, P., Söderberg, O., Grummt, I., et al. (2005). c-Myc associates with ribosomal
922 DNA and activates RNA polymerase I transcription. Nat Cell Biol *7*, 303-310.
923 10.1038/ncb1225.
924 6. Grandori, C., Gomez-Roman, N., Felton-Edkins, Z.A., Ngouenet, C., Galloway, D.A.,
925 Eisenman, R.N., and White, R.J. (2005). c-Myc binds to human ribosomal DNA and
926 stimulates transcription of rRNA genes by RNA polymerase I. Nat Cell Biol *7*, 311-318.
927 10.1038/ncb1224.
928 7. Rossetti, S., Hoogeveen, A.T., Esposito, J., and Sacchi, N. (2010). Loss of MTG16a
929 (CBFA2T3), a novel rDNA repressor, leads to increased ribogenesis and disruption of
930 breast acinar morphogenesis. J Cell Mol Med *14*, 1358-1370. 10.1111/j.1582-
931 4934.2009.00982.x.
932 8. Rossetti, S., Wierzbicki, A.J., and Sacchi, N. (2016). Mammary epithelial
933 morphogenesis and early breast cancer. Evidence of involvement of basal
934 components of the RNA Polymerase I transcription machinery. Cell Cycle *15*, 2515-
935 2526. 10.1080/15384101.2016.1215385.
936 9. Eilbracht, J., Kneissel, S., Hofmann, A., and Schmidt-Zachmann, M.S. (2005). Protein
937 NO52--a constitutive nucleolar component sharing high sequence homologies to
938 protein NO66. Eur J Cell Biol *84*, 279-294. 10.1016/j.ejcb.2004.12.022.
939 10. Tsuneoka, M., Koda, Y., Soejima, M., Teye, K., and Kimura, H. (2002). A novel myc
940 target gene, mina53, that is involved in cell proliferation. J Biol Chem *277*, 35450-
941 35459. 10.1074/jbc.M204458200.
942 11. Bundred, J.R., Hendrix, E., and Coleman, M.L. (2018). The emerging roles of
943 ribosomal histidyl hydroxylases in cell biology, physiology and disease. Cellular and
944 molecular life sciences : CMLS *75*, 4093-4105. 10.1007/s00018-018-2903-z.
945 12. Chowdhury, R., Sekirnik, R., Brissett, N.C., Krojer, T., Ho, C.H., Ng, S.S., Clifton, I.J.,
946 Ge, W., Kershaw, N.J., Fox, G.C., et al. (2014). Ribosomal oxygenases are structurally
947 conserved from prokaryotes to humans. Nature *510*, 422-426. 10.1038/nature13263.
948 13. Ge, W., Wolf, A., Feng, T., Ho, C.H., Sekirnik, R., Zayer, A., Granatino, N., Cockman,
949 M.E., Loenarz, C., Loik, N.D., et al. (2012). Oxygenase-catalyzed ribosome
950 hydroxylation occurs in prokaryotes and humans. Nat Chem Biol *8*, 960-962.
951 10.1038/nchembio.1093.
952 14. Yanshina, D.D., Gopanenko, A.V., Karpova, G.G., and Malygin, A.A. (2020).
953 [Replacement of Hydroxylated His39 in Ribosomal Protein uL15 with Ala or Thr Impairs
954 the Translational Activity of Human Ribosomes]. Mol Biol (Mosk) *54*, 512-521.
955 10.31857/s0026898420030209.
956 15. Yu, M., Sun, J., Thakur, C., Chen, B., Lu, Y., Zhao, H., and Chen, F. (2014).
957 Paradoxical roles of mineral dust induced gene on cell proliferation and
958 migration/invasion. PLoS One *9*, e87998. 10.1371/journal.pone.0087998.

16. Komiya, K., Sueoka-Aragane, N., Sato, A., Hisatomi, T., Sakuragi, T., Mitsuoka, M., Sato, T., Hayashi, S., Izumi, H., Tsuneoka, M., and Sueoka, E. (2010). Expression of Mina53, a novel c-Myc target gene, is a favorable prognostic marker in early stage lung cancer. Lung Cancer *69*, 232-238. 10.1016/j.lungcan.2009.10.010.
17. Jaffe, A.B., Kaji, N., Durgan, J., and Hall, A. (2008). Cdc42 controls spindle orientation to position the apical surface during epithelial morphogenesis. J Cell Biol *183*, 625-633. 10.1083/jcb.200807121.
18. Sambuy, Y., De Angelis, I., Ranaldi, G., Scarino, M.L., Stammati, A., and Zucco, F. (2005). The Caco-2 cell line as a model of the intestinal barrier: influence of cell and culture-related factors on Caco-2 cell functional characteristics. Cell Biol Toxicol *21*, 1-26. 10.1007/s10565-005-0085-6.
19. MacCallum, A., Hardy, S.P., and Everest, P.H. (2005). Campylobacter jejuni inhibits the absorptive transport functions of Caco-2 cells and disrupts cellular tight junctions. Microbiology (Reading) *151*, 2451-2458. 10.1099/mic.0.27950-0.
20. Srinivasan, B., Kolli, A.R., Esch, M.B., Abaci, H.E., Shuler, M.L., and Hickman, J.J. (2015). TEER measurement techniques for in vitro barrier model systems. J Lab Autom *20*, 107-126. 10.1177/2211068214561025.
21. Tsuneoka, M., Nishimune, Y., Ohta, K., Teye, K., Tanaka, H., Soejima, M., Iida, H., Inokuchi, T., Kimura, H., and Koda, Y. (2006). Expression of Mina53, a product of a Myc target gene in mouse testis. Int J Androl *29*, 323-330. 10.1111/j.1365-2605.2005.00572.x.
22. Andersen, J.S., Lam, Y.W., Leung, A.K., Ong, S.E., Lyon, C.E., Lamond, A.I., and Mann, M. (2005). Nucleolar proteome dynamics. Nature *433*, 77-83. 10.1038/nature03207.
23. Scott, M.S., Troshin, P.V., and Barton, G.J. (2011). NoD: a Nucleolar localization sequence detector for eukaryotic and viral proteins. BMC Bioinformatics *12*, 317. 10.1186/1471-2105-12-317.
24. Scott, M.S., Boisvert, F.M., McDowall, M.D., Lamond, A.I., and Barton, G.J. (2010). Characterization and prediction of protein nucleolar localization sequences. Nucleic Acids Res *38*, 7388-7399. 10.1093/nar/gkq653.
25. Chytła, A., Gajdzik-Nowak, W., Olszewska, P., Biernatowska, A., Sikorski, A.F., and Czogalla, A. (2020). Not Just Another Scaffolding Protein Family: The Multifaceted MPPs. Molecules *25*. 10.3390/molecules25214954.
26. Ye, F., Zeng, M., and Zhang, M. (2018). Mechanisms of MAGUK-mediated cellular junctional complex organization. Curr Opin Struct Biol *48*, 6-15. 10.1016/j.sbi.2017.08.006.
27. Hanada, T., Takeuchi, A., Sondarva, G., and Chishti, A.H. (2003). Protein 4.1-mediated membrane targeting of human discs large in epithelial cells. J Biol Chem *278*, 34445-34450. 10.1074/jbc.M305209200.
28. Feng, T., Yamamoto, A., Wilkins, S.E., Sokolova, E., Yates, L.A., Munzel, M., Singh, P., Hopkinson, R.J., Fischer, R., Cockman, M.E., et al. (2014). Optimal translational termination requires C4 lysyl hydroxylation of eRF1. Molecular cell *53*, 645-654. 10.1016/j.molcel.2013.12.028.
29. Markolovic, S., Zhuang, Q., Wilkins, S.E., Eaton, C.D., Abboud, M.I., Katz, M.J., McNeil, H.E., Lesniak, R.K., Hall, C., Struwe, W.B., et al. (2018). The Jumonji-C oxygenase JMJD7 catalyzes (3S)-lysyl hydroxylation of TRAFAC GTPases. Nat Chem Biol *14*, 688-695. 10.1038/s41589-018-0071-y.
30. Verrastro, I., Pasha, S., Jensen, K.T., Pitt, A.R., and Spickett, C.M. (2015). Mass Spectrometry-Based Methods for Identifying Oxidized Proteins in Disease: Advances and Challenges. Biomolecules *5*, 378-411.
31. Cockman, M.E., Lippl, K., Tian, Y.M., Pegg, H.B., Figg, W.D.J., Abboud, M.I., Heilig, R., Fischer, R., Myllyharju, J., Schofield, C.J., and Ratcliffe, P.J. (2019). Lack of activity of recombinant HIF prolyl hydroxylases (PHDs) on reported non-HIF substrates. Elife *8*. 10.7554/eLife.46490.

1013 32. Perdivara, I., Deterding, L.J., Przybylski, M., and Tomer, K.B. (2010). Mass
1014 spectrometric identification of oxidative modifications of tryptophan residues in
1015 proteins: chemical artifact or post-translational modification? J Am Soc Mass Spectrom
1016 *21*, 1114-1117. 10.1016/j.jasms.2010.02.016.
1017 33. Cockman, M.E., Lancaster, D.E., Stolze, I.P., Hewitson, K.S., McDonough, M.A.,
1018 Coleman, M.L., Coles, C.H., Yu, X., Hay, R.T., Ley, S.C., et al. (2006).
1019 Posttranslational hydroxylation of ankyrin repeats in IkappaB proteins by the hypoxia-
1020 inducible factor (HIF) asparaginyl hydroxylase, factor inhibiting HIF (FIH). Proceedings
1021 of the National Academy of Sciences of the United States of America *103*, 14767-
1022 14772. 10.1073/pnas.0606877103.
1023 34. Coleman, M.L., McDonough, M.A., Hewitson, K.S., Coles, C., Mecinovic, J.,
1024 Edelmann, M., Cook, K.M., Cockman, M.E., Lancaster, D.E., Kessler, B.M., et al.
1025 (2007). Asparaginyl hydroxylation of the Notch ankyrin repeat domain by factor
1026 inhibiting hypoxia-inducible factor. The Journal of biological chemistry *282*, 24027-
1027 24038. 10.1074/jbc.M704102200.
1028 35. Yang, M., Chowdhury, R., Ge, W., Hamed, R.B., McDonough, M.A., Claridge, T.D.,
1029 Kessler, B.M., Cockman, M.E., Ratcliffe, P.J., and Schofield, C.J. (2011). Factor-
1030 inhibiting hypoxia-inducible factor (FIH) catalyses the post-translational hydroxylation
1031 of histidinyl residues within ankyrin repeat domains. The FEBS journal *278*, 1086-
1032 1097. 10.1111/j.1742-4658.2011.08022.x.
1033 36. Yang, M., Ge, W., Chowdhury, R., Claridge, T.D., Kramer, H.B., Schmierer, B.,
1034 McDonough, M.A., Gong, L., Kessler, B.M., Ratcliffe, P.J., et al. (2011). Asparagine
1035 and aspartate hydroxylation of the cytoskeletal ankyrin family is catalyzed by factor-
1036 inhibiting hypoxia-inducible factor. The Journal of biological chemistry *286*, 7648-7660.
1037 10.1074/jbc.M110.193540.
1038 37. Moreno-García, M.E., Sommer, K., Shinohara, H., Bandaranayake, A.D., Kurosaki, T.,
1039 and Rawlings, D.J. (2010). MAGUK-controlled ubiquitination of CARMA1 modulates
1040 lymphocyte NF-kappaB activity. Mol Cell Biol *30*, 922-934. 10.1128/mcb.01129-09.
1041 38. Ploumakis, A., and Coleman, M.L. (2015). OH, the Places You'll Go! Hydroxylation,
1042 Gene Expression, and Cancer. Molecular cell *58*, 729-741.
1043 10.1016/j.molcel.2015.05.026.
1044 39. Islam, M.S., Leissing, T.M., Chowdhury, R., Hopkinson, R.J., and Schofield, C.J.
1045 (2018). 2-Oxoglutarate-Dependent Oxygenases. Annu Rev Biochem *87*, 585-620.
1046 10.1146/annurev-biochem-061516-044724.
1047 40. Wu, V.M., Yu, M.H., Paik, R., Banerjee, S., Liang, Z., Paul, S.M., Bhat, M.A., and Beitel,
1048 G.J. (2007). Drosophila Varicose, a member of a new subgroup of basolateral
1049 MAGUKs, is required for septate junctions and tracheal morphogenesis. Development
1050 *134*, 999-1009. 10.1242/dev.02785.
1051 41. Moyer, K.E., and Jacobs, J.R. (2008). Varicose: a MAGUK required for the maturation
1052 and function of Drosophila septate junctions. BMC Dev Biol *8*, 99. 10.1186/1471-213x-
1053 8-99.
1054 42. Stucke, V.M., Timmerman, E., Vandekerckhove, J., Gevaert, K., and Hall, A. (2007).
1055 The MAGUK protein MPP7 binds to the polarity protein hDlg1 and facilitates epithelial
1056 tight junction formation. Mol Biol Cell *18*, 1744-1755. 10.1091/mbc.e06-11-0980.
1057 43. Qin, Y., Capaldo, C., Gumbiner, B.M., and Macara, I.G. (2005). The mammalian
1058 Scribble polarity protein regulates epithelial cell adhesion and migration through E-
1059 cadherin. J Cell Biol *171*, 1061-1071. 10.1083/jcb.200506094.
1060 44. Xue, B., Krishnamurthy, K., Allred, D.C., and Muthuswamy, S.K. (2013). Loss of Par3
1061 promotes breast cancer metastasis by compromising cell-cell cohesion. Nat Cell Biol
1062 *15*, 189-200. 10.1038/ncb2663.
1063 45. Buckley, A., and Turner, J.R. (2018). Cell Biology of Tight Junction Barrier Regulation
1064 and Mucosal Disease. Cold Spring Harb Perspect Biol *10*.
1065 10.1101/cshperspect.a029314.

46. Krug, S.M., Schulzke, J.D., and Fromm, M. (2014). Tight junction, selective permeability, and related diseases. Semin Cell Dev Biol *36*, 166-176. 10.1016/j.semcdb.2014.09.002.
47. Sawada, N. (2013). Tight junction-related human diseases. Pathol Int *63*, 1-12. 10.1111/pin.12021.
48. Chen, Y., Yang, X., Huang, Y., Liu, E., and Wang, L. (2011). Associations of the single-nucleotide polymorphisms of the Mina gene with the development of asthma in Chinese Han children: a case-control study. Genet Test Mol Biomarkers *15*, 531-536. 10.1089/gtmb.2010.0240.
49. Mori, T., Okamoto, K., Tanaka, Y., Teye, K., Umata, T., Ohneda, K., Tokuyama, K., Okabe, M., and Tsuneoka, M. (2013). Ablation of Mina53 in mice reduces allergic response in the airways. Cell Struct Funct *38*, 155-167. 10.1247/csf.13006.
50. Pillai, M.R., Mihi, B., Ishiwata, K., Nakamura, K., Sakuragi, N., Finkelstein, D.B., McGargill, M.A., Nakayama, T., Ayabe, T., Coleman, M.L., and Bix, M. (2019). Myc-induced nuclear antigen constrains a latent intestinal epithelial cell-intrinsic anthelmintic pathway. PLoS One *14*, e0211244. 10.1371/journal.pone.0211244.
51. McKay, D.M., Shute, A., and Lopes, F. (2017). Helminths and intestinal barrier function. Tissue Barriers *5*, e1283385. 10.1080/21688370.2017.1283385.
52. Bąska, P., and Norbury, L.J. (2022). The Role of the Intestinal Epithelium in the "Weep and Sweep" Response during Gastro-Intestinal Helminth Infections. Animals (Basel) *12*. 10.3390/ani12020175.
53. Hanahan, D., and Weinberg, R.A. (2011). Hallmarks of cancer: the next generation. Cell *144*, 646-674. 10.1016/j.cell.2011.02.013.
54. Martin, T.A., and Jiang, W.G. (2009). Loss of tight junction barrier function and its role in cancer metastasis. Biochim Biophys Acta *1788*, 872-891. 10.1016/j.bbamem.2008.11.005.
55. Thakur, C., and Chen, F. (2015). Current understanding of mdig/MINA in human cancers. Genes Cancer *6*, 288-302. 10.18632/genesandcancer.73.
56. Xu, F., Si, X., Du, J., Xu, F., Yang, A., Zhang, C., Zhang, X., and Yang, Y. (2019). Downregulating SynCAM and MPP6 expression is associated with ovarian cancer progression. Oncol Lett *18*, 2477-2483. 10.3892/ol.2019.10542.
57. Tseng, T.C., Marfatia, S.M., Bryant, P.J., Pack, S., Zhuang, Z., O'Brien, J.E., Lin, L., Hanada, T., and Chishti, A.H. (2001). VAM-1: a new member of the MAGUK family binds to human Veli-1 through a conserved domain. Biochim Biophys Acta *1518*, 249-259. 10.1016/s0167-4781(01)00191-9.
58. Schmidt, H., Würl, P., Taubert, H., Meye, A., Bache, M., Holzhausen, H.J., and Hinze, R. (1999). Genomic imbalances of 7p and 17q in malignant peripheral nerve sheath tumors are clinically relevant. Genes Chromosomes Cancer *25*, 205-211.
59. Wong, K.F., So, C.C., and Kwong, Y.L. (1999). Chronic myelomonocytic leukemia with t(7;11)(p15;p15) and NUP98/HOXA9 fusion. Cancer Genet Cytogenet *115*, 70-72. 10.1016/s0165-4608(99)00085-0.
60. Parada, L.A., Hallén, M., Tranberg, K.G., Hägerstrand, I., Bondeson, L., Mitelman, F., and Johansson, B. (1998). Frequent rearrangements of chromosomes 1, 7, and 8 in primary liver cancer. Genes Chromosomes Cancer *23*, 26-35. 10.1002/(sici)1098-2264(199809)23:1<26::aid-gcc5>3.3.co;2-g.
61. Miozzo, M., Perotti, D., Minoletti, F., Mondini, P., Pilotti, S., Luksch, R., Fossati-Bellani, F., Pierotti, M.A., Sozzi, G., and Radice, P. (1996). Mapping of a putative tumor suppressor locus to proximal 7p in Wilms tumors. Genomics *37*, 310-315. 10.1006/geno.1996.0565.
62. Grundy, R.G., Pritchard, J., Scambler, P., and Cowell, J.K. (1998). Loss of heterozygosity for the short arm of chromosome 7 in sporadic Wilms tumour. Oncogene *17*, 395-400. 10.1038/sj.onc.1201927.
63. Powlesland, R.M., Charles, A.K., Malik, K.T., Reynolds, P.A., Pires, S., Boavida, M., and Brown, K.W. (2000). Loss of heterozygosity at 7p in Wilms' tumour development. Br J Cancer *82*, 323-329. 10.1054/bjoc.1999.0922.

1121 64. Murakami, Y. (2005). Involvement of a cell adhesion molecule, TSLC1/IGSF4, in
1122 human oncogenesis. Cancer Sci *96*, 543-552. 10.1111/j.1349-7006.2005.00089.x.
1123 65. Sakurai-Yageta, M., Masuda, M., Tsuboi, Y., Ito, A., and Murakami, Y. (2009). Tumor
1124 suppressor CADM1 is involved in epithelial cell structure. Biochem Biophys Res
1125 Commun *390*, 977-982. 10.1016/j.bbrc.2009.10.088.
1126 66. Sun, S., Liu, W., and Li, Y. (2020). CADM1 enhances intestinal barrier function in a rat
1127 model of mild inflammatory bowel disease by inhibiting the STAT3 signaling pathway.
1128 J Bioenerg Biomembr *52*, 343-354. 10.1007/s10863-020-09850-8.
1129 67. Ferreira, R., Schneekloth, J.S., Jr., Panov, K.I., Hannan, K.M., and Hannan, R.D.
1130 (2020). Targeting the RNA Polymerase I Transcription for Cancer Therapy Comes of
1131 Age. Cells *9*. 10.3390/cells9020266.
1132 68. Krissinel, E., and Henrick, K. (2004). Secondary-structure matching (SSM), a new tool
1133 for fast protein structure alignment in three dimensions. Acta Crystallogr D Biol
1134 Crystallogr *60*, 2256-2268. 10.1107/s0907444904026460.
1135 69. Emsley, P., and Cowtan, K. (2004). Coot: model-building tools for molecular graphics.
1136 Acta Crystallogr D Biol Crystallogr *60*, 2126-2132. 10.1107/s0907444904019158.
1137 70. Mirdita, M., Schütze, K., Moriwaki, Y., Heo, L., Ovchinnikov, S., and Steinegger, M.
1138 (2022). ColabFold: making protein folding accessible to all. Nat Methods *19*, 679-682.
1139 10.1038/s41592-022-01488-1.
1140